6.5. Recommendations based upon physics issues

1) The single-null divertor operating with the density in the scrape-off $\gtrsim 5 \times 10^{19}$ m^{-3} should be retained as the reference concept for INTOR. Further studies of the physics are needed.
2) The pumped limiter if operated in a similar density regime is an attractive alternative, and continued attention should be devoted to this concept.
3) Despite the merits of limiter operation with a radiative plasma edge (either due to injected or to sputtered impurities), the concept is one of high risk. Until this issue is resolved it is premature to state a preference for the low- or high-radiation edge condition or the applicability of low- or high-atomic-number plate material.

REFERENCES TO CHAPTER VI

[1] INTOR GROUP, International Tokamak Reactor: Zero Phase (Rep. Int. Tokamak Reactor Workshop Vienna, 1979) International Atomic Energy Agency, Vienna (1980). See also Summary in Nucl. Fusion 20 (1980) 349.
[2] INTOR GROUP, International Tokamak Reactor: Phase One (Rep. Int. Tokamak Reactor Workshop, 1980–81), International Atomic Energy Agency (1982). See also Summary in Nucl. Fusion 22 (1982) 135.
[3] European Community Contributions to the INTOR Phase-Two-A Workshop, Rep. Commission of the European Communities, Brussels (1982).
[4] Japan Contribution to the INTOR Phase-Two-A Workshop, Rep. Japan Atomic Energy Research Institute, Tokai-mura (1982).
[5] USA Contribution to the INTOR Phase-Two-A Workshop, Rep. FED-INTOR/82-1, Georgia Institute of Technology, Atlanta (1982).
[6] USSR Contribution to the INTOR Phase-Two-A Workshop, Rep. Kurchatov Institute, Moscow (1982).

Chapter VII

IMPURITY CONTROL AND FIRST-WALL ENGINEERING

M.A. ABDOU – USA
T. HIRAOKA – Japan
H. IIDA – Japan
R.F. MATTAS – USA
P. SCHILLER – EC
D.V. SEREBRENNIKOV – USSR
G.E. SHATALOV – USSR

1. INTRODUCTION

The critical issues effort for the INTOR impurity control system involved an integrated study of the key physics and engineering aspects of the divertor and limiter. The results of the physics-related effort were summarized in the previous chapter. This chapter is devoted to the engineering-related considerations. The most critical engineering problem for the limiter and divertor plate is the lifetime, which tends to be short because of the combination of high erosion rates and the relatively small allowable thickness of the plasma-side materials. Serious effort was devoted to an assessment of the limiter and divertor lifetime for a wide range of potential plasma operating conditions and a large number of candidate materials and design concepts.

The key erosion mechanisms investigated included physical and chemical sputtering and vaporization and loss of the melt layer during plasma disruptions. The rate of erosion by physical sputtering is strongly dependent on the plasma scrape-off conditions. Therefore, the choice of materials and design concepts was evaluated for three plasma edge temperature regimes: low ($T_s < 50$ eV), medium ($T_s \approx 100$–200 eV) and high ($T_s > 700$ eV), where T_s is the pre-sheath temperature at the limiter or divertor plate. The physics evaluation of these edge temperature regimes was presented in the previous chapter. The physics operating conditions used for the engineering evaluation are summarized in Section 2. Models were developed to evaluate the re-deposition of materials eroded from the limiter and divertor plate. These models and estimates of the net erosion and re-deposition rates are presented in Section 9.

A data base assessment was conducted for the surface and bulk properties of candidate materials for the limiter, divertor and first wall. A summary of this assessment is given in Section 4.

The main design concept for the limiter and divertor plates utilizes a duplex-type wall in which the plasma-side materials, in the form of tiles, are attached to a heat sink that provides for heat removal and structural support. Significant effort was devoted to determining the maximum allowable thickness of the tiles. As discussed in Sections 2 and 3, shaping of the limiter and inclining of the divertor plates relative to the magnetic field lines were found necessary in order to reduce the peak heat flux and to increase the allowable tile thickness to acceptable levels. Concepts for attaching the tiles to the heat sink are described in Section 5. The results of the thermal hydraulics and stress analyses are discussed in Section 6. The design considerations related to electromagnetic forces induced during plasma disruptions are analysed in Section 7. The thermal response of candidate materials to plasma disruptions is summarized in Section 8.

Section 10 presents the results of the lifetime analysis for various candidate materials under different plasma operating conditions. Section 11 presents the major features of the design concepts recommended for the limiter and divertor.

The integration of the physics and engineering considerations in this study made it possible to derive a number of important conclusions and recommendations concerning the impurity control system in tokamaks. These conclusions and the recommendations for future effort are summarized in Sections 12 and 13.

This chapter attempts to summarize only the key results. More detailed analyses and documentation of the data base are available in the reports of the four national contributions [1–4].

2. OPERATING CONDITIONS

2.1. Common parameters

The plasma performance, reactor operating scenario, disruption conditions, and some engineering parameters are common to both the limiter and divertor. These parameters are presented in Table VII-1. The plasma parameters and operating scenario are unchanged from the Phase-One INTOR report [5].

Several disruption scenarios were considered in Phase Two A. The reference disruption parameters are shown in Tables VII-1 and VII-2. The total of the thermal plasma energy and poloidal field energy is 290 MJ. The field energy, 60 MJ, is assumed to be deposited uniformly on the plasma chamber wall in the form of radiation for both the limiter and divertor options. For the limiter/divertor reference conditions 80 MJ is deposited on 30% of the first wall with an added peaking factor of two, and another 80 MJ goes to the limiter or divertor collector

TABLE VII-1. COMMON OPERATING PARAMETERS

Stage	I	II	III
Plasma			
Thermonuclear power (MW)	620	620	620
α-power (MW)	124	124	124
Neutron power (MW)	496	496	496
Neutron wall loading ($MW \cdot m^{-2}$)	1.3	1.3	1.3
Operating scenario			
Years of operation	3	4	8
Availability (%)	13.3	25	50
Cycle time (s)	146	246	246
Burn time (s)	100	200	200
Total burn time (s)	8.7×10^6	25.6×10^6	103×10^6
Total cycles	8.7×10^4	12.8×10^4	51.5×10^4
Total neutron fluence	1.5×10^{28}	5.5×10^{28}	22.1×10^{28}
Integral wall loading ($MW \cdot a \cdot m^{-2}$)	0.3	1	4.2
Disruptions			
(Major disruptions)			
Frequency	5×10^{-3}	10^{-3}	10^{-3}
Disruptions/year	165	31	62
Total disruptions	495	124	496
Total energy (MJ)	290	290	290
Thermal plasma energy (MJ)	230	230	230
Field energy (MJ)	60	60	60
Disruption time			
Poloidal field (ms)	20	20	20
Plasma current (ms)	20	20	20
Thermal energy (ms)			
Reference	20	20	20
Alternate	5	5	5
(Minor disruptions)			
Frequency	10^{-2}	5×10^{-3}	5×10^{-3}
Disruptions/year	330	155	310
Total disruptions	990	620	2480
Total energy to limiter/divertor (MJ)	50	50	50
Disruption time			
Thermal energy (ms)			
Reference	20	20	20
Alternate	5	5	5
Engineering (all stages)			
Plasma chamber surface area (m^2)	380		
Limiter/divertor location	Bottom of chamber		
Configuration	24 separately removable modules each weighing $\approx$25 Mg		
Pumping system	Compound cryopumps located below nuclear island		
Desired lifetime	$\gtrsim$2 years, 50% availability		
Coolant	H_2O, $<100^\circ C$		

TABLE VII-2. LIMITER/DIVERTOR DISRUPTION CHARACTERISTICS

	Peak energy density ($J \cdot cm^{-2}$)[a]
MAJOR DISRUPTIONS	
Case 1: divertor case	
First wall	170
Divertor plate	230
Case 2: high load to limiter	
First wall	35
Limiter	535
Case 3: reasonable load to limiter	
First wall	170
Limiter	270
MINOR DISRUPTIONS	
Case 1: divertor	
Divertor plate	170
Case 2: limiter	
Limiter	170

[a] The area of the limiter blade or divertor collector plates is about 50 m^2.

plate. The energy to the limiter/divertor is assumed to have the same spatial distribution as the operating heat loads. The remaining 70 MJ of thermal energy is uniformly deposited on the plasma chamber wall in the form of radiation. The resultant peak energy loads are shown in Table VII-2. A high-load option has also been considered for the limiter where 160 MJ is deposited on the limiter, and the remaining energy is uniformly deposited on the wall.

Specifications have been established for minor disruptions. The minor disruptions are characterized by a relatively high frequency of occurrence but a reduced thermal-energy deposition. The minor disruption is 50 MJ to either the divertor or limiter, with the same spatial distribution as the operating heat loads.

The limiter and divertor are both placed at the bottom of the plasma chamber. The limiter/divertor modules are designed to be removed separately from the rest of the blanket because of the relatively short lifetime anticipated for these components. The primary configurational differences are the changes in the poloidal-field coil current distribution and in the power supplies required for the divertor option.

Of particular importance to the work in this chapter is to correlate the energy of ions incident on the divertor/limiter surface to the plasma temperature (T_s) in front of the neutralizer plate, which is discussed in the previous chapter. Accounting for a sheath potential of about $3T_s$, the average D/T ion energy at the plate is about 4.5 T_s. The charge state of the ions, which are sputtered from the plate, ionized and returned to it, is critical in determining their accelerated energy. The charge state is discussed in the previous chapter and is found to be 2–3 for low-Z materials and 3–4 for high-Z materials in the range of electron temperatures at the plate of 20–100 eV. Therefore, the ion energy of impurities striking the divertor/limiter surface is 7–10 T_s for low-Z and 10–13 T_s for high-Z materials.

2.2. Divertor/first wall

2.2.1. Low temperature at divertor plate

The overall divertor design is very similar to the Phase-One divertor design [5]. The divertor heat and particle fluxes are shown in Table VII-3. For the low-temperature condition (T_s = 30 eV) the energy of DT ions striking the collector plate is only 135 eV. The ions have a reduced energy due to increased radiation losses along the divertor channel. The low ion temperature also results in a somewhat reduced heat load on the collector plates which is compensated by an increased heat load on the divertor throat.

2.2.2. Medium temperature at divertor plate

The operating parameters for the medium-edge-temperature concept are also shown in Table VII-3. The energy of the D or T ions striking the collector plate is 400 eV. The charge state of impurity ions returning to the divertor plate is about 3 to 4. Therefore, the energy of the impurity ions ($\approx$ 1200–1600 eV) is probably above the point where high-Z materials may be used because of excessive self-sputtering, and a low-Z material should be used on the surface.

2.3. Limiter/first wall

2.3.1. Low edge temperature

The limiter heat and particle fluxes are shown in Table VII-4. For the low-temperature condition, most of the α-heating power is radiated uniformly from the plasma edge to the first wall, and the ion heat load to the limiter is low. The energies of ions and neutrals striking the limiter are low enough that high-Z materials, with low sputtering coefficients, may be used.

TABLE VII-3. HEAT AND PARTICLE FLUXES FOR THE DIVERTOR OPTION (HIGH-EDGE-DENSITY CONDITION)

	Low T at plate	Medium T at plate
Divertor		
Scrape-off temperature (eV)	100	100
Plasma density in scrape-off layer (m^{-3})	5×10^{19}	5×10^{19}
Temperature at plate (eV)	30	100
Total energy to divertor (MW)	80	80
Ions only on divertor plates (MW)	52	54
Electrons only on divertor plate (MW)	18	18
Average energy of ions on divertor plate (eV)	135	450
Ion flux on the two divertor plates (s^{-1})	2.4×10^{24}	7.5×10^{23}
Power load on divertor throat area and other divertor walls		
Charge-exchange load (total) (MW)	4	2
Energy of neutrals (eV)	120	200
Neutral flux (total) (s^{-1})	2×10^{23}	6×10^{22}
Peaking factor of deposition load	2	2
Radiation (MW)	6	6
Area of divertor throat and other divertor walls on which neutrals impinge: 5 strips of 0.2 m each, 4 of them being adjacent to the ends of the divertor plates and the fifth on the wall facing the outside divertor plate, adjacent to the pumping duct (total) (m^2)	33	33
First wall (uniform distribution)		
Radiation (MW)	40	40
Charge exchange (MW)	4	4
Average energy of charge-exchange neutrals (eV)	100	100
Neutral-particle flux (consisting of hydrogen atoms) (s^{-1})	2.5×10^{23}	2.5×10^{23}
Charged-particle power flux	negligible	negligible
Scrape-off width for power flow (midplane) (cm)	1.9	1.9

2.3.2. Medium edge temperature

The operating parameters for the medium-edge-temperature design are given in Table VII-4. The edge temperature of 150 eV is, at present, believed to be the most easily attainable operating regime. The D or T ion energy (edge energy plus sheath potential) is 615 eV. Since the charge state of impurity ions returning to the limiter is about 3 to 4, the energy of the impurity ions is high enough to require the use of low-Z materials on the limiter surface. The ion energy at the leading edges is low enough that high-Z materials can be considered, however.

TABLE VII-4. HEAT AND PARTICLE FLUXES FOR THE LIMITER OPTION

Parameter	Low T (High radiation)	Medium T	High T
Alpha heating (MW)	124	124	124
Radiation (MW)	112	40	20
Ions to limiter (MW)	8	45	60
Electrons to limiter (MW)	4	15	20
Neutrals to limiter (MW)	–	20	20
Neutrals to wall (MW)	0.5	4	4
Limiter ion flux (s^{-1})	6×10^{23}	1.25×10^{24}	7.2×10^{22}
Limiter neutral flux (s^{-1})	–	4.2×10^{23}	4.3×10^{22}
Wall neutral flux (s^{-1})[a]	1.6×10^{23}	8.3×10^{22}	8.6×10^{21}
DT ion energy (eV)	45	675	4300
Neutral energy (eV)	20	300	2900
Edge electron temperature (eV)[b]	10	150	670
Edge density (m^{-3})[b]	5×10^{19}	2.5×10^{19}	5×10^{18}
e-folding distances (cm)			
Temperature[c]	2	2	2
Power[c]	1.5	1.5	1.5
Density[c]	long	long	long

[a] The neutral wall flux falls on two 0.5 m, poloidal-width, strips at each end of the limiter.
[b] At the 'point of tangency'.
[c] At midplane.

2.3.3. High edge temperature

The operating parameters for the high edge temperature are also given in Table VII-4. The power radiated and transported to the first wall and limiter are the same as for the medium-edge-temperature concept. For low-Z materials, high edge temperatures are more desirable than the medium edge temperature because they are beyond the energy for peak sputtering. It is, however, concluded that the realization of the high-edge-temperature condition is sufficiently uncertain that it would be imprudent to base the design on this condition.

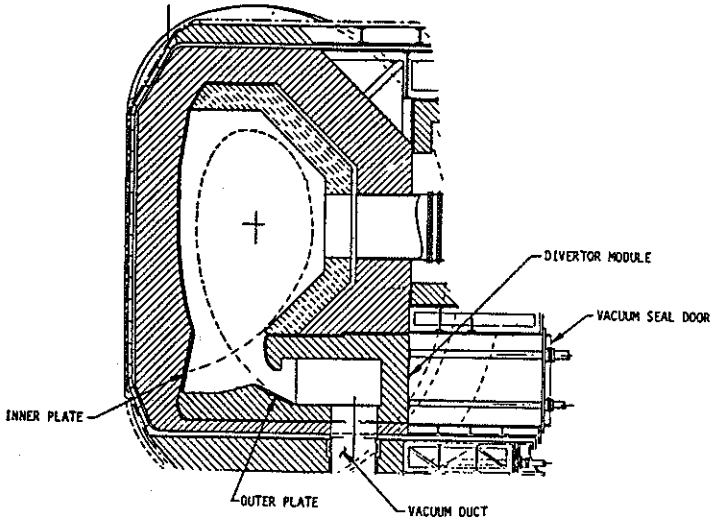

FIG. VII-1. Divertor configuration (reference design).

3. MECHANICAL CONFIGURATION

During Phase Two A the pumped limiter has been introduced as an option for impurity control. A double-edged shaped toroidal limiter located at the bottom of the plasma chamber has been selected as the limiter reference design. The configuration of the divertor has remained the same as in Phase One.

3.1. Divertor

The overall configuration of the poloidal divertor concept is shown in Fig. VII-1. The divertor is located at the bottom of the plasma chamber with a continuous toroidal opening extending around the reactor. The divertor is divided into removable modules. There are 24 modules, two for each TF coil. These modules are removable so the divertor collector plates can be replaced without removing an entire torus sector. This is required because it is anticipated that replacement of the divertor collector plates will be more frequent than that of the first wall. Access limitations of 12 TF coils require the use of two modules per sector to allow removal. The divertor module does not incorporate breeding at this time, but this can be included if required.

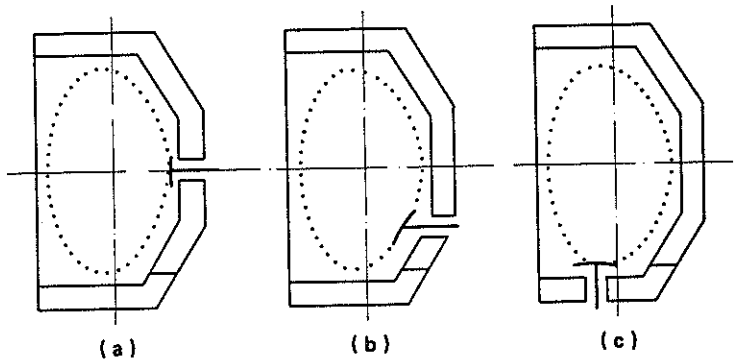

FIG. VII-2. Pumped-limiter positions.

The divertor collector plates are set at an angle with respect to the magnetic field lines in order to limit the peak heat flux to about 2 $MW \cdot m^{-2}$. For the inner channel, which has a peak heat flux of 4 $MW \cdot m^{-2}$ normal to the separatrix, the plate is placed at an angle of 30° to the field lines. For the outer channel, which has a peak heat flux of 8 $MW \cdot m^{-2}$ normal to the separatrix, the plate is placed at an angle of about 15° to the field lines. Shaping of the collector plates could produce a constant heat flux over a portion of the surface, but a compound curvature would be required. Since the peak heat flux is already manageable, shaping does not appear to be necessary. The details can be obtained from Phase-One report [5].

3.2. Pumped limiter

3.2.1. Location

Different locations for the pumped limiter have been compared, namely (Fig. VII-2):

- at the bottom of the plasma chamber, as for the divertor case (2c)
- at the midplane (2a)
- at an intermediate position (2b)m 45% lower quarter position.

The criteria identified to select the most convenient location have been the following:

- effect on tritium breeding
- consequences on reactor layout, operation and maintenance
- possibility of uniform distribution of thermal loads.

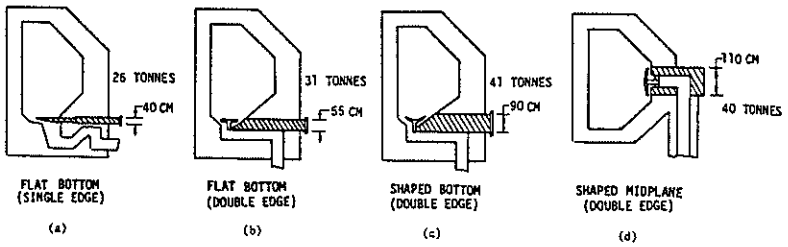

FIG. VII-3. Pumped-limiter shape options.

From the point of view of tritium breeding, it has been shown that the various positions are comparable. A midplane limiter potentially reduces the size of the TF coils by allowing the blanket/shield to be symmetrical in the vertical direction. In addition, the magnetic configuration is simplified. However, the midplane location is in an area where heating systems, diagnostics and test modules are likely to be located. Furthermore, the midplane limiter will require a longer vacuum duct which could limit access to the lower half of the blanket and shield. Concerning the heat and particle flow, the bottom location appears to offer more flexibility. The particle and energy e-folding distances are greater at the bottom location. For a flat limiter, the peak heat fluxes are expected to be lowest at the bottom location. Finally, the bottom limiter minimizes the reactor design changes coming from a single-null poloidal divertor design, and makes comparison with the divertor easier. Therefore, the bottom location has been selected as the reference design case for the limiter.

3.2.2. Limiter shape

The limiter has to provide for pumping of the gaseous ashes from the plasma. It is exposed to a very high heat flux. The need to be effective in pumping and the necessity for an acceptable lifetime are the primary considerations in determining the form of the limiter.

Proposed solutions for the limiter blade are one or two leading edges and various shapes of its surface. In Fig. VII-3, some possible solutions are presented. Concepts (a) and (b) are flat limiters while concepts (c) and (d) are contoured. Concept (a) has a single leading edge while all other concepts have two leading edges. The primary difference between the single- and the double-edged designs is the additional pumping capability of the double-edged design. For a given pumping speed, the leading edges of the double-edged limiter can be placed further away from the plasma edge than for a single-edged design. This reduces the heat

load to the leading edge. The reduced heat load will result in an increased lifetime for the leading edge.

Different forms of limiters have been discussed, the simplest being a flat plate inserted on the bottom of the plasma chamber. The heat distribution on this limiter will be strongly peaked. The same is, of course, true for the sputtering. Therefore, other shapes of the limiter plate have been proposed, which can assure a more uniform distribution of the heat flux density.

Most solutions consider a limiter design with a heat sink covered by a protection plate. The fabrication of such a duplex structure presents problems as already discussed during Phase One in the case of the divertor. Therefore, other solutions may present advantages.

3.2.2.1. The plate limiter

The distribution of the heat flux on the limiter surface depends on the geometrical form of the plate. Three possibilities have been examined: a flat plate, a plate with a constant radius and a plate contoured in a way that the heat flux density is constant over the whole surface.

The heat flux, $\dot{q}$, to the limiter surface facing the plasma is given approximately by

$$\dot{q} = \frac{\dot{Q}_T}{4\pi R\lambda_Q} \exp(-Z/\lambda_Q) \sin\theta \qquad (1)$$

where $\dot{Q}_T$ is the total particle-transported heat load, R the major radius to the limiter, λ_Q the heat flux e-folding distance, Z the radial distance from the limiter surface to the plasma edge, and θ the angle of incidence between the limiter and poloidal flux lines. A circular plasma will be assumed for developing analytical expressions relating the various parameters in Eq. (1).

The flat limiter

For a flat limiter, Eq. (1) can be approximated by

$$\dot{q}(\chi) = \frac{\dot{Q}_T}{4\pi R\lambda_Q} \left(\frac{\chi}{a}\right) \exp\left(\frac{-\chi^2}{2a\lambda_Q}\right) \qquad (2)$$

where a is the minor radius.

Equation (2) represents a symmetric heat flux distribution with a low heat flux density in the centre of the plate, two peaks and an exponentially falling density towards the edges. However, the angle at the leading edges between the

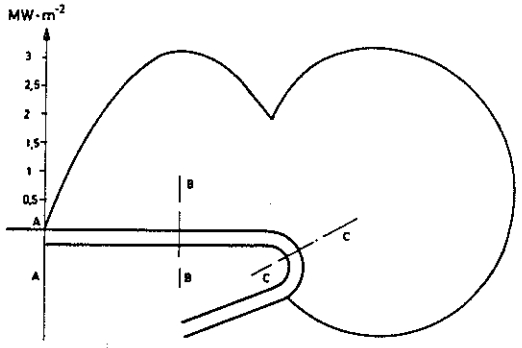

FIG. VII-4. Heat flux density on a flat limiter.

incoming particles and the surfaces increases and, therefore, there are further peaks at the leading edges (Fig. VII-4).

The concave limiter

The form of the heat flux distribution on a concave limiter with a constant curvature is essentially the same as for a flat one. But, depending on the radius, the values of the heat flux are reduced (Fig. VII-5).

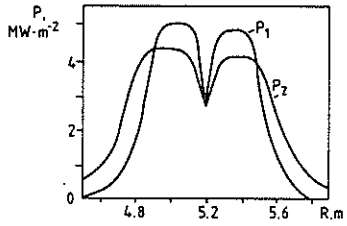

FIG. VII-5. Heat flux distribution over the limiter surface: 1 – flat limiter, 2 – concave limiter.

The contoured limiter

To obtain a constant heat flux along the limiter, the quantity $\dot{q}$ in Eq. (1) has to be made a constant. Figure VII-6 gives the form of a limiter surface constructed in this way.

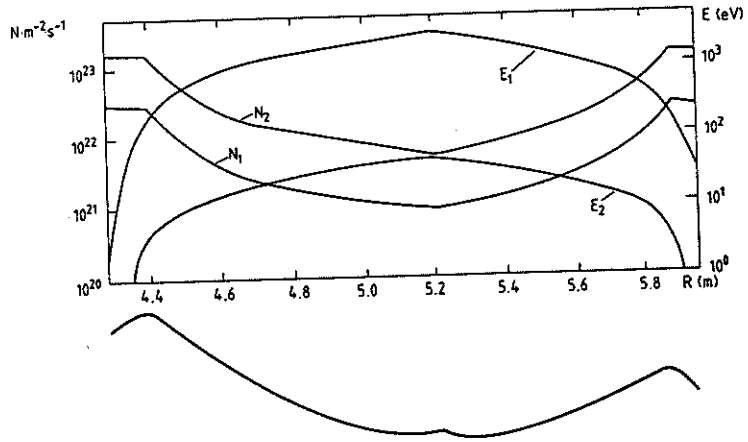

FIG. VII-6. Distribution of particle flows and their energy on the surface of the limiter with uniform thermal load ($P = 2$ MW·m^{-2}): 1 – high-temperature mode, 2 – low-temperature mode.

Changes of the horizontal position of the plasma with respect to the limiter change the heat deposition. For a displacement of 3 cm, the maximum change of heat deposition is about ±0.9 MW·m^{-2} in the centre of the limiter subjected to 80 MW total power. The influence of the e-folding length on the changes is not very strong.

The particle flux distribution on the limiter is given by an expression similar to Eq. (1) but with different constants. The particle flux density on the limiter contoured for constant heat flux is not constant but increases towards the ends of the limiter plates (Fig. VII-6). The increase in particle flux density at the limiter surface can result in a sputtering erosion at the edges that is much higher than in the centre of the limiter. However, together with the particle flux, there is also a decrease in the particle energy across the scrape-off layer. At particle energies below 400 eV, the sputtering coefficient for all particles decreases with the particle energy. In this case, the increase in particle flux density is partly counterbalanced by the decrease of the sputtering coefficient. In the case of low edge temperature, the particle energy at the tip falls below the threshold energy for sputtering, and the tips have no sputtering erosion. If the particle energies are higher than the peak energy, then the decrease in particle energy means an increase in the sputtering coefficient and, finally, an enhancement of the sputtering rates at the edges of the limiter plates.

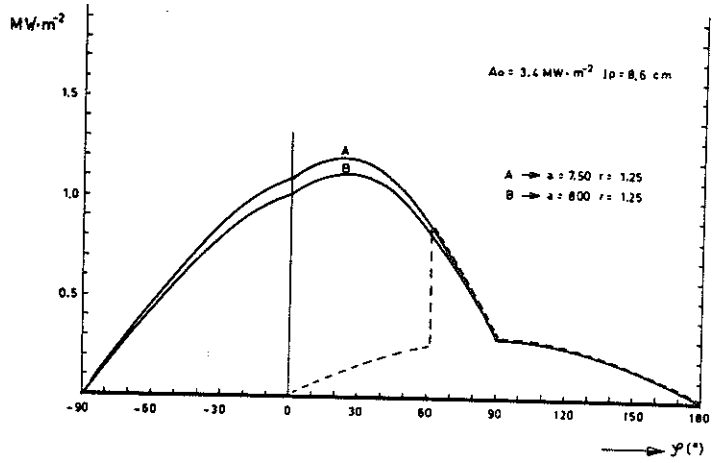

FIG. VII-7. Heat load to tubes in the scrape-off layer (r = 1.25 cm): —— edge tube, – – tube in the row. 90° is the direction to the plasma centre.

3.2.2.2. The tube limiter

Heat exchangers composed of tubes are quite common, due to the advantages of the geometry of the tubes [1]. Therefore, it has been attempted to design a limiter based on an array of tubes for the low-edge-temperature case. The tube limiter seems to be easy to build and to have a low sensitivity to variations of the plasma position. A row of tubes may replace the limiter plate. The arrangement could be on a straight line or in a more triangular form. Since the tube limiter cannot take advantage of the possibility of a constant heat flux density, on each tube separately, the arrangement can be made to satisfy other conditions, such as, e.g. the most effective width of the pumping channel or to be withdrawn with minimum impact on the blanket.

There are two distinct heat fluxes arriving at the limiters in the case of low edge temperature. The first one is the radiation heat flux crossing the separatrix perpendicularly. Its total value amounts to 112 MW. This gives an average value of 0.3 $MW \cdot m^{-2}$ on any surface facing the plasma.

The second flux arriving at the limiter is the ion and electron flux parallel to the separatrix (12 MW). The power of this flux parallel to the separatrix decreases exponentially with the distance from the separatrix. The scale length of the exponential function depends on the magnetic configuration and varies along the separatrix. Figure VII-7 gives the heat flux distribution on a tube in the row and at the leading edge.

3.3. First wall

The load on the first wall has been considerably changed with respect to Phase One in the new scenarios described in Section 2. In all limiter cases, the sputtering on the first wall has become negligible except for the strips in the region of the edges. The first wall has, therefore, to cope only with disruption erosion and heat flux. For the cases with high and medium edge temperatures no large problems arise. However, the low-edge-temperature case includes a very high heat load and therefore considerable fatigue problems.

The first wall near the leading edges will be exposed to considerable erosion by charge-exchanged neutrals. Special measures for its protection or frequent exchange are necessary.

The divertor cases have been discussed extensively during Phase One.

4. MATERIALS CONSIDERATIONS

A materials data base assessment has been conducted as part of the Impurity Control and First-Wall Engineering task. The purpose of this assessment is to evaluate and develop a data base for candidate materials for the first wall, limiter and divertor. Recommended values for critical materials properties are provided for use in the design activity. Uncertainties in the materials data base have been determined so that the impact on critical design parameters can be evaluated. The limiting features and favourable characteristics of the primary candidate materials are summarized.

This assessment has focused primarily on (1) materials that will be exposed directly to the plasma, and (2) candidate heat-sink materials for use in the pumped-limiter and divertor applications. Candidate plasma-side materials include low-Z (atomic number), medium-Z and high-Z materials listed in Table VII-5. A greater emphasis was placed on the bold-face typed materials in the table. Properties considered include physical sputtering by energetic plasma particles and wall-eroded materials (self-sputtering), chemical sputtering, H/He retention/release, and critical bulk materials properties including radiation effects.

4.1. Plasma-side materials

4.1.1. Physical sputtering

The present assessment has focused on defining the energy-dependent sputtering yields for the light plasma particles (D, T, He) and the self-sputtering yields for the primary candidate wall materials, including selected compounds. Considerable experimental data on light-ion (D, He) sputtering for normal incidence

TABLE VII-5. CANDIDATE LIMITER/DIVERTOR MATERIALS

Plasma-side materials	
Low-Z:	C, Be, B, TiC, SiC, B_4C, BeO
Medium-Z:	Stainless steel, V
High-Z:	W, Ta, Nb, Mo
Heat sink materials	
Copper alloy	
Zirconium alloy	
Vanadium alloy	
Niobium alloy	

The assessment of the heat sink materials has focused primarily on copper alloys with a high thermal conductivity, zirconium alloys, and vanadium alloys. Properties evaluated include physical and mechanical properties, corrosion/compatibility, radiation effects and fabrication characteristics.

have been generated in recent years. Many of these data are available in two compilations [6, 7]. Variations in reported sputtering yields for similar systems have generally been attributed to differences in experimental methods (measurements of erosion yield), possible contamination effects (particularly for oxygen active materials such as beryllium and aluminium, and differences in surface condition or microstructure of the wall material. Although significant differences exist in the data base for certain materials, trends in the data base can generally be obtained within an uncertainty of a factor of two. Several analytical models have been developed to provide estimates of the sputtering yields for materials and conditions for which data do not exist. These models are particularly useful for predicting tritium sputtering yields and self-sputtering yields, both of which are dominant contributors to the wall erosion. For light ions, two empirical models [8, 9] provide the best correlations with existing data for energy-dependent sputtering yields and, therefore, are recommended as a basis for the present INTOR study. Details of the sputtering models, designated IPP and DSPUT, are presented in Refs [8, 9].

Figures VII-8 to VII-12 show a comparison of the energy-dependent sputtering yields predicted by the IPP and DSPUT codes with some of the experimental data for the primary candidate materials. The models generally give good agreement with the experimental light-ion sputtering data for the primary candidate materials.

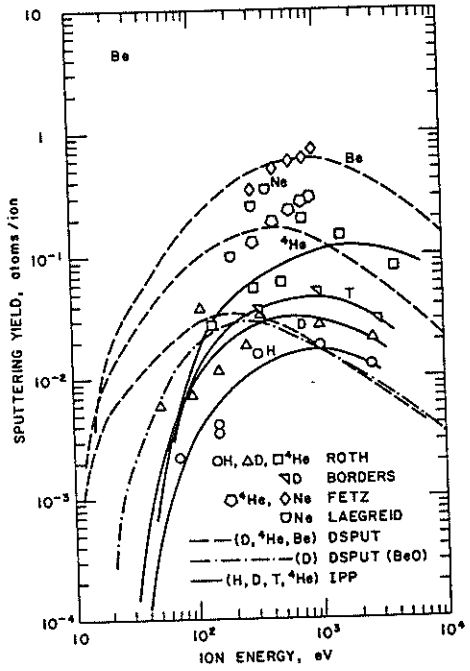

FIG. VII-8. Energy-dependent physical sputtering yields for beryllium.

The reported light-ion sputtering data for beryllium are very similar to those for BeO. It is generally believed that the beryllium was contaminated with oxygen and that the reported beryllium data are indicative of an oxide film on beryllium. Therefore, the sputtering yield predicted by the DSPUT code for beryllium is believed to be a better estimate of the yield for beryllium than the experimental data. Very few data exist for self-sputtering. Therefore, the models are based primarily on sputtering data for inert-gas ions of similar mass. The results indicate that the self-sputtering yields (normal incidence) do not exceed unity for low-Z materials such as beryllium and graphite. The predicted self-sputtering yields for most high-Z materials such as vanadium, iron (stainless steel), molybdenum and tungsten exceed unity at incident particle energies of 400 – 800 eV. Therefore, incident particle energies must be maintained below these levels to avoid a propagating erosion effect if the sputtered wall material is ionized and accelerated back to the wall by a sheath potential as predicted (see Section 9). For incident particles with intermediate mass numbers (20–40), the uncertainty in the

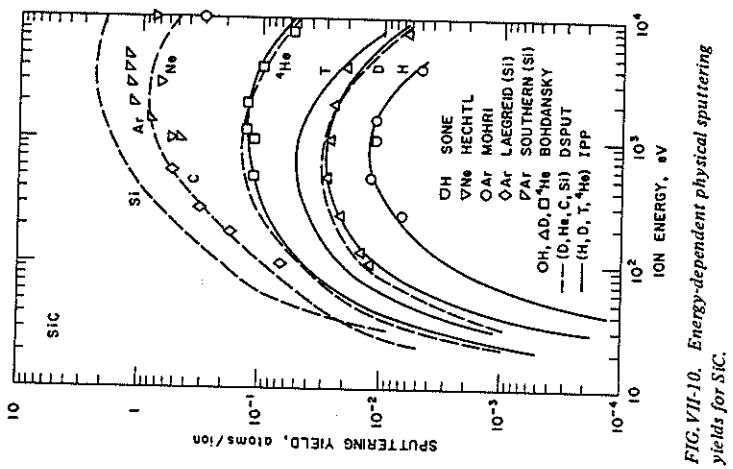

FIG. VII-10. Energy-dependent physical sputtering yields for SiC.

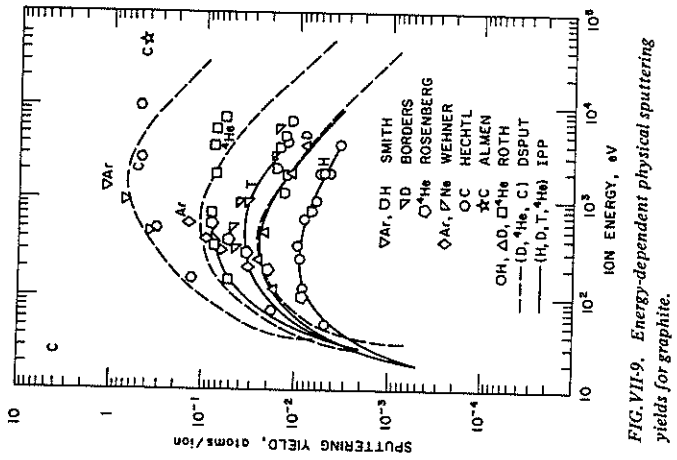

FIG. VII-9. Energy-dependent physical sputtering yields for graphite.

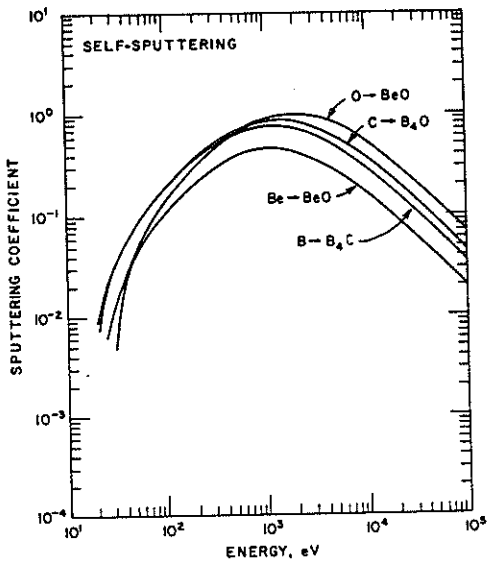

FIG. VII-11. Calculated (DSPUT) energy-dependent self-sputtering yields for BeO and B_4C.

sputtering yield data is too large to allow a reliable determination of whether self-sputtering yields will exceed unity. As indicated in Fig. VII-10 for SiC, the DSPUT code predicts a maximum yield less than unity for carbon but greater than unity for silicon. Experimental data for neon (M = 20) give maximum yields slightly less than unity whereas the maximum yields for argon (M = 40) are slightly greater than unity. On the basis of these uncertainties, it is not possible to determine whether SiC will give self-sputtering yields greater or less than unity. The maximum self-sputtering yields for BeO are believed to be less than unity.

4.1.2. Chemical sputtering

Possible chemical interactions that lead to wall erosion by chemical sputtering have been evaluated. The primary effort is on hydrogen (D or T) effects on graphite. Hydrogen (D or T) effects on candidate carbides (B_4C, SiC, and TiC) have also been assessed. Oxygen impurities may also cause chemical sputtering of reactive materials. This aspect has been evaluated primarily in terms of tungsten; however, extrapolation to other metals can be made.

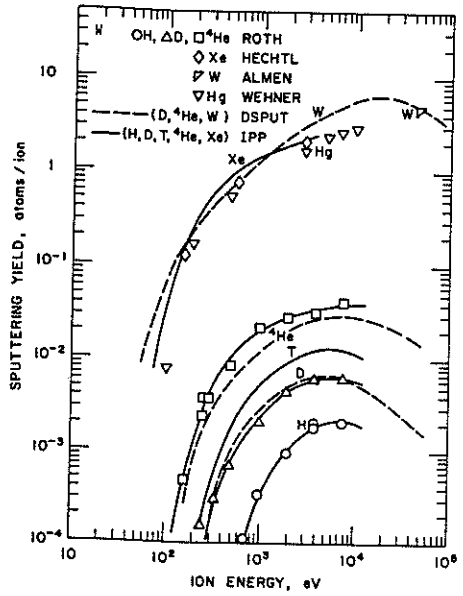

FIG. VII-12. Energy-dependent physical sputtering yields for tungsten.

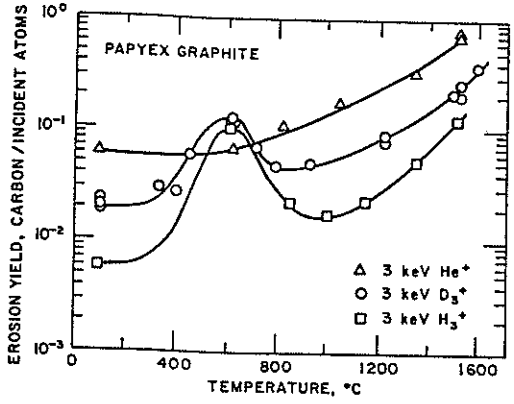

FIG. VII-13. Temperature dependence of chemical sputtering yield of papyex graphite.

Most investigations of chemical sputtering of graphite by light-ion bombardment have focused on the formation of methane. Methane is formed in the temperature range between 200° and 800°C and increases the graphite sputtering yield well above that observed for physical sputtering only. The maximum methane formation rate has been shown to occur at a temperature of about 550° – 600°C and about 1 keV incident hydrogen ion energy. Until recently, not much attention was paid to studies of graphite erosion by hydrogen bombardment at temperatures above 700°C. Figure VII-13 (see Ref. [10]) shows the sputtering yield of carbon for 1-keV H^+ and D^+ incident ions and for 3-keV He^+ ions at temperatures to 1600°C. While an erosion peak is observed at 525°C for carbon bombardment by H^+ and D^+, no peak is detected during helium bombardment at that temperature. However, a rapid rise in sputtering is seen at temperatures above 700°C for all three incident ions H^+, D^+ and He^+. These high erosion rates indicate that a mechanism other than classical physical or chemical sputtering must be present as no hydrocarbon formation was observed at these high temperatures [10]. Several possible mechanisms are being considered at present.

Simultaneous electron and hydrogen bombardment has been shown to increase the sputtering rate of graphite. Figure VII-14 shows the temperature dependence of sputtering for the carbon base alloy USB-15 which has been simultaneously bombarded with 20-keV H_2^+ ions and 400-eV electrons [11]; chemical sputtering effects are observed to 200°C, but large effects are observed for temperatures $\gtrsim$400°C. At 450°C, the sputtering coefficient observed for simultaneous H_2^+ ion and electron bombardment is approximately five times higher than the coefficient observed with H_2^+ ion bombardment alone. Evidently, electron irradiation contributes to the carbon atom chemical bonds, and thus enhances CH_4 formation.

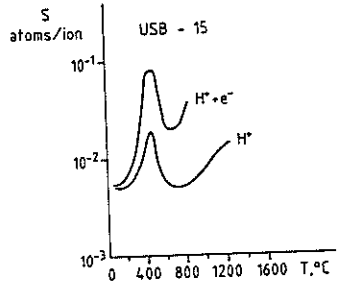

FIG. VII-14. Temperature dependence of sputtering for carbon-based alloy USB-15 irradiated by H_2^+ ions at 20 keV and simultaneously by H_2^+ ions and electrons at 400 eV.

The effects of the chemical sputtering of carbides, e.g. B_4C, SiC and TiC, are much smaller than those observed in the case of graphite. Based upon limited data, a chemical erosion yield a factor of two higher than the physical sputtering yield for energetic hydrogen has been observed at temperatures of 500–650°C for SiC. The peak chemical sputtering yield for B_4C, which is similar to that of SiC, occurs at a temperature of about 200°C. The TiC appears to be less sensitive to chemical sputtering by hydrogen than are SiC or B_4C.

Chemical sputtering on surfaces of tungsten centres on the effects of oxygen on tungsten erosion rates. It has been shown that there are several stages of oxygen adsorption on the tungsten surface. Below monolayer coverage, oxygen is adsorbed on the tungsten surface in the absence of tungsten oxide formation. As the amount of oxygen is increased above monolayer coverage, tungsten oxides begin to form. These oxides have a much higher volatility and can therefore be expected to drastically enhance the erosion of tungsten surfaces during light-ion bombardment. When tungsten surfaces are covered with just a monolayer of oxygen, erosion of tungsten is suppressed. Computer calculations have shown that the sputtering yield for tungsten decreases two to four times, depending on the incident ions and their energy, when the surface is covered with a monolayer of oxygen.

4.1.3. Arcing

Unipolar arcing is a concern at high plasma edge temperatures for the limiter and divertor collector plates. Arcing occurs with almost all materials although, in general, a marked reduction is observed for metals with higher melting points and for good insulators. The use of insulators would probably require coated plates, and this is discussed later after first considering metals. Arcing with metals also very strongly depends on surface conditions.

Samples of various materials and specific surface preparations have been exposed to the plasma, and arcing has been observed with bias voltages between 6 and 500 V. For a typical stainless-steel sample, several thousand arc craters with diameters of about 30 μm were observed on the surface. From the crater dimensions and the current signal, an average erosion rate of $\Delta m/\Delta Q = 5 \times 10^{-5}$ $g \cdot C^{-1}$ has been estimated, corresponding fairly well to the erosion rate data of vacuum arcs.

Under given plasma parameters and fixed bias voltage, the arcing probability has been found to be a strong function of the surface state of the sample. Experience gained with various sample materials and surface conditions is summarized in Fig. VII-15, which shows the number of arcs per unit area as a function of sample material and surface preparation. The arcing rate has been measured as a function of time, and in all cases an exponential decay has been observed, indicating that the number of arcing sites was finite for given surface and plasma conditions. Increasing the bias voltage, however, activated additional arcing sites which did not show up at low bias. Some more recent data of importance to the present problem are reproduced in Fig. VII-16. These measurements were taken as part of the testing of low-Z refractory coatings for fusion reactor limiters [12]. Several points are obvious from Fig. VII-16: according to these measurements, the erosion rates for Mo and W are the lowest: approximately, 0.001 times that for stainless. Be and TiC are other candidate materials. Of these, erosion for Be is about 5 times that for TiC, both being of the same order of magnitude as stainless. Arcing of coating material depends strongly on the method of application; e.g. plasma spray (P.S.) coatings of TiC eroded about five times as fast as CVD coatings. Other materials of interest, e. g. BeO and BeC were not tested but are expected to be somewhat better than Be (however, the fact that TiC does not appear better than Ti places some doubt on this hypothesis).

Recent results from tokamak experiments indicate that a sheath electric field of about 3×10^7 $V \cdot m^{-1}$ is required to initiate arcing. This field value appears to be independent of the materials tested, which include Mo, SiC, TiC, Be, C, Al, and stainless steel [13].

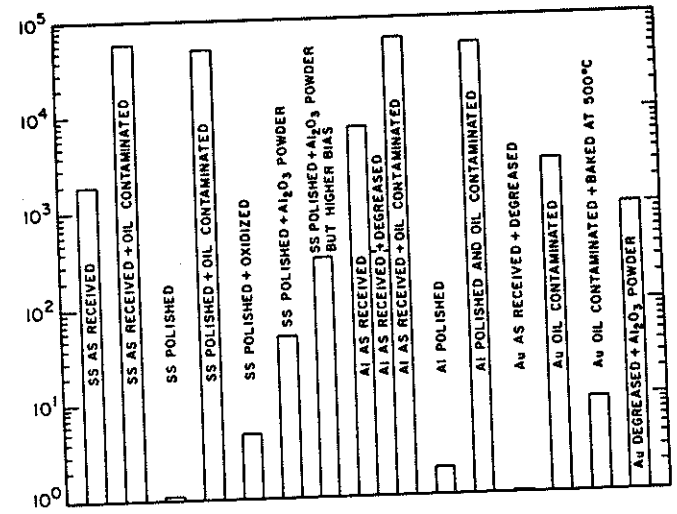

FIG. VII-15. Number of arcs per unit area as a function of sample material and surface preparation.

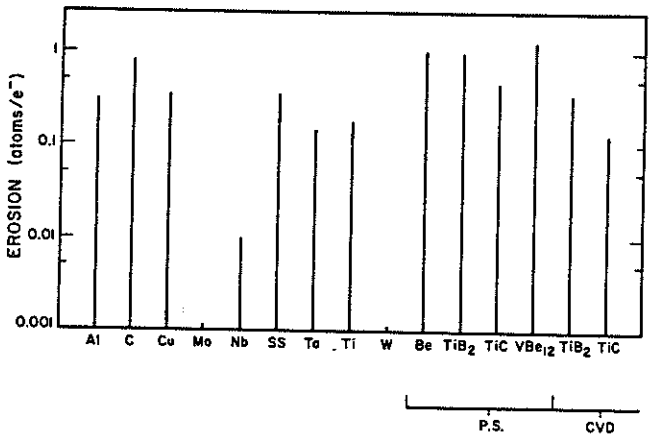

FIG. VII-16. Arc erosion rates for a variety of test materials.

4.1.4. H/He retention/release

The hydrogen and helium retention and release characteristics of the plasma-side materials are important considerations in the selection of limiter/divertor materials. Hydrogen (DT) retention/release characteristics affect the tritium inventory in the wall and the tritium permeation into the coolant and may affect the mechanical integrity of the wall materials. Detailed analyses of the tritium retention/release from candidate wall materials are presented in Chapter VIII. The focus of the present study is on the impact of energetic hydrogen (DT) and helium injected into the surface of the first-wall, limiter and divertor materials.

Hydrogen retention and release for a material is generally assumed to be governed by diffusion, defect trapping, and the molecular recombination rate at the surface. Metals with an endothermic hydrogen heat of solution and reasonably high solubility (e.g. stainless steel) exhibit relatively weak trapping, while endothermic metals with low hydrogen solubility (e.g. Cu) typically have trap binding energies $\gtrsim$1 eV, causing high hydrogen retention as a result of the precipitation of hydrogen bubbles. The rate of release of hydrogen from an endothermic metal is often dominated by diffusion and detrapping at low temperatures. However, molecular recombination can become the rate-limiting step for hydrogen release at higher temperatures. The temperature for the transition from diffusion and detrapping-limited kinetics to recombination-limited kinetics is materials-dependent. Metals with an exothermic hydrogen heat of solution (e.g. V, Ta) often show hydride precipitation at low temperatures and high

hydrogen retention in solid solution at higher temperatures, controlled by recombination-limited kinetics. Finally, trapping and release of hydrogen in non-metals such as carbon and carbides is characterized by high concentrations of strong traps. In general, diffusivities and solubilities are not well known for non-metals. Temperatures above $\approx$600°C are required for release of hydrogen from graphite and the carbides.

Helium release in metals is uniformly characterized by low migration energies ($\lesssim$0.4 eV), high trapping energies ($\gtrsim$2 eV), and high saturation concentrations (up to a He/metal ratio of about 0.4). Once the available traps are saturated, additional implanted helium is rapidly released. Helium trapping in non-metals such as TiC appears at least qualitatively similar to the trapping observed in metals. Little is known about hydrogen-helium synergistic effects, although for metals with low hydrogen solubilities (e.g. beryllium) the hydrogen and helium appear to compete for the limited number of available trapping sites.

Temperature limits for acceptable release must be established for the candidate materials. The analyses indicate that the temperature gradient established in the wall by the surface heat flux tends to reduce tritium permeation compared to the case with a uniform wall temperature, because of the lowered temperature at the coolant side, and in the case of stainless steel, because of thermal diffusion to the hot side of the wall (Soret effect). Tritium barriers on the coolant side of the wall will theoretically reduce the tritium permeation through the wall. Oxide films characteristic of those on many metals, e.g. stainless steel, exposed to elevated temperature water will tend to reduce the tritium permeation. The data base for tritium permeation barriers should be extended to other materials and to INTOR-like conditions.

4.1.5. Bulk properties and radiation effects

4.1.5.1. Low-Z materials

The focus of the data-base assessment for the low-Z materials is on beryllium, graphite, silicon carbide and beryllium oxide. The critical materials properties for these materials are summarized in Table VII-6. Beryllium has a very low atomic number, good thermal conductivity and heat capacity and relatively high heats of vaporization and fusion. Graphite has many attractive properties including a high sublimation temperature. The vaporization rate becomes excessive at temperatures above $\approx$2000 K. Although graphite has a relatively high thermal conductivity at low temperatures, the conductivity is rapidly reduced at relatively low radiation levels ($<$1 dpa). Silicon carbide also tends to decompose and vaporize before melting and, therefore, avoids the melt layer problem during disruptions. However, the maximum operation temperature (1700 K) and the thermal shock resistance of SiC are generally lower than those for graphite. As shown in Table VII-6, a

TABLE VII-6. PROPERTY VALUES AT 800 K FOR LOW-Z MATERIALS

Property (units)	Property value				
	Be	BeO	C	SiC	SiC high K
Melting temperature (K)	1557	2823	–	–	–
Sublimation temperature at 10^{-2} Pa(K)	–	–	2300	1800	1800
Density[a] ($Mg \cdot m^{-3}$)	1.85	3.01	1.8[b]	3.20	3.20
Thermal expansion, 300–800 K (10^{-6} K^{-1})	15.90	8.20	4.20	4.90	4.70
Thermal conductivity ($W \cdot mK^{-1}$)					
unirradiated	103	66	103	37	90 (est.)
irradiated[c]	103	36	25	9	–
Specific heat ($J \cdot kg^{-1} \cdot K^{-1}$)	2250	1840	1620	1150	–
Young modulus (GPa)					
unirradiated	190	36	8	400	380
irradiated	–	–	18	400	–
Yield strength (MPa)					
unirradiated	90	76	14[d]	360	220
irradiated[c]	110	–	21[d]	360	–
Elongation, irradiated[c] (%)	5	<1	<1	<1	–

[a] Density at 30 K.
[b] Density of graphite ranges up to 2.25 $Mg \cdot m^{-3}$ depending on product form.
[c] High-fluence irradiation properties.
[d] Tensile strength for graph-N3M is about 470 MPa (unirradiated), estimated 230 MPa after high-fluence irradiation.

high-thermal-conductivity SiC (BeO-doped) has recently been produced [2] with increased thermal shock resistance. BeO has a high thermal conductivity at low temperatures, a high melting temperature and is not believed to be susceptible to chemical sputtering.

The non-metals C, SiC and BeO all have relatively high thermal conductivities at low temperature. However, relatively low radiation doses tend to severely reduce the conductivity of these types of materials. Although considerable effort has been expended to develop high-conductivity SiC, it is not clear that the high conductivity can be maintained in the radiation environment. Figure VII-17 shows the effect of radiation doses on the conductivity of SiC as a function of temperature. The thermal conductivities of these types of materials generally decrease significantly as the temperature is increased above room temperature.

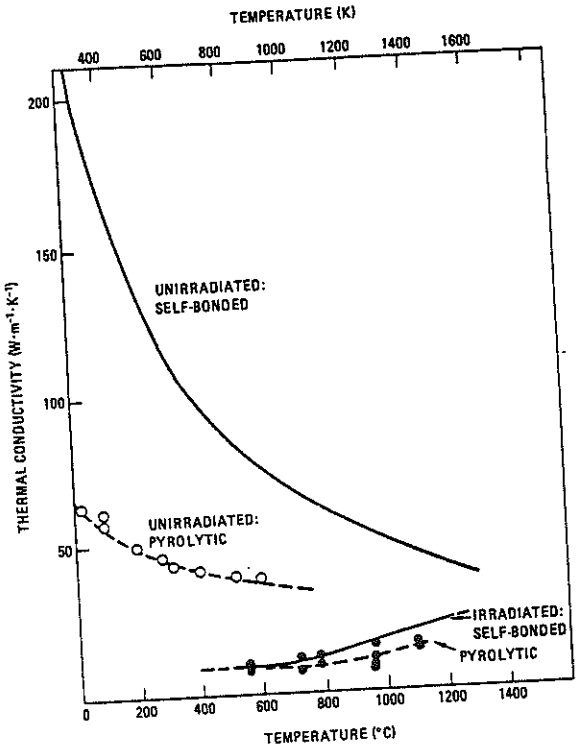

FIG. VII-17. Thermal conductivity of unirradiated SiC and irradiated SiC at the irradiation temperature as a function of temperature (fluences between 10^{25} and 10^{26} $n \cdot m^{-2}$).

For example, the thermal conductivity of the CVD SiC is about a factor of two higher (67 $W \cdot mK^{-1}$) at 25°C than at 525°C. Under irradiation, the conductivity tends to become insensitive to temperature at values slightly below the high temperature values.

4.1.5.2. High-Z materials

Tungsten, tantalum, and molybdenum are of interest for the plasma-side materials because of their low light-ion sputtering yields, their relatively high threshold energy for sputtering by deuterium and tritium and their relatively high energy (≈700 eV) at which self-sputtering exceeds unity. Values for the

TABLE VII-7. PROPERTIES OF HIGH-Z MATERIALS AT 500 K

Property	W	Ta	Mo
Atomic weight	184	181	94
Density ($g \cdot cm^{-3}$)	19.25	16.6	10.2
Melting point (K)	3683	3269	2883
Thermal expansion ($\times 10^{-6} K^{-1}$)	4.2	6.6	5.5
Thermal conductivity ($W \cdot m^{-1} \cdot K^{-1}$)	145	61.8	120
Heat capacity ($J \cdot kg^{-1} \cdot K^{-1}$)	138	148	251
Modulus of elasticity (GPa)	398	176	306

physical properties of tantalum, tungsten, and molybdenum at temperatures in the range of interest are summarized in Table VII-7. Only limited data exist on the effects of radiation on the properties of tungsten, tantalum, and molybdenum. The ductile-brittle transition temperature (DBTT) of tungsten is increased from 65 to 230°C after fast reactor irradiation at 385°C to fluences of $(4-9) \times 10^{25} n \cdot m^{-2}$. At higher fluences $(1.5-4.4) \times 10^{26} n \cdot m^{-2}$) and similar temperatures, the uniform elongation of tantalum was reduced to ≈0.1% with a total elongation of 8–10%. No relevant fatigue data for tungsten were found in the literature. Limited data indicate excellent low-cycle fatigue resistance of tantalum at temperatures below 732°C.

4.1.6. Re-deposited material

Sputtering calculations (see Section 9) predict that sputtered particles from the limiter or divertor are re-deposited on the surface. In some areas, a net erosion, in others a net growth of material is predicted. The structure and properties of re-deposited materials may be different from the underlying substrate, and therefore the operation of the impurity control system could be affected. This section summarizes the evaluation of re-deposited material.

Since there are no experimental data on the properties of re-deposited materials, their characteristics have been assumed to be equivalent to thin films produced by conventional vapour deposition. The growth mode of thin films can conveniently be determined from the Movchan-Demchishin (M–D) model which describes the microstructural morphology of thin films as a function of the substrate temperature, and which has been verified for the deposition of a number of pure metals. According to the M–D model, at deposition (substrate) temperatures lower than 0.3 T_m, where T_m is the melting point of the depositing species, the

deposit grows as tapered crystallites that form from a limited number of nuclei. The structure is not fully dense and contains longitudinal porosity. At deposition temperatures between about 0.3 and 0.5 T_m, increasing surface mobility with increasing temperature results in fully dense columnar grains. At temperatures above 0.5 T_m, increasing bulk diffusion results in an equi-axed, recrystallized grain structure.

The surface temperatures of beryllium and tungsten are estimated to vary from 200 to 700°C, depending on the material thickness. T_m, 0.5 T_m, and 0.3 T_m for beryllium and tungsten are, respectively, 1280, 500 and 200°C, and 3380, 1550, and 820°C. Based on the M–D model, Be deposits are expected to be recrystallized and equi-axed for a flat limiter and to be composed of dense columnar grains for a curved limiter. In the case of tungsten, the deposits on both types of limiters are expected to be porous and composed of tapered crystallites. Furthermore, re-deposition occurs under energetic ion bombardment which tends to eliminate the columnar growth morphology and promotes greater density and an equi-axed structure. Thus, under typical reactor conditions, re-deposited beryllium can be expected to be fully dense and equi-axed. W deposits are expected to be less than fully dense (≈30% porosity).

Deposit durability depends on the deposit/substrate adhesion which in turn is determined by the nature of the deposit/substrate interface. For self-substrate deposition of pure metals such as beryllium and tungsten, no interface reactions occur and the microstructure and properties can be expected to be continuous across the interface. The porosity in W deposits might slightly decrease deposit durability.

The physical and mechanical properties are expected to vary with the microstructure and thickness of the deposits. It is anticipated that the physical properties, such as thermal conductivity, will approach bulk values for thicknesses above ≈0.1 μm. The mechanical properties of the re-deposited materials are more difficult to predict. In the case of thick Be films (75–100 μm), the strength and ductility vary with the deposition temperature. For deposition temperatures of 350–425°C, the room-temperature tensile strength has been measured to be 135 MPa, and the elongation has been measured to be only 0.1%. For deposition temperatures of 760–790°C, the room-temperature tensile strength increases to ≈290 MPa, and the elongation increases to 1%.

W deposits are more complex, since the ductile-brittle transition temperature (DBTT) and the mechanical properties are sensitive functions of the microstructure, particularly grain size and morphology, and interstitial impurities. The properties of W deposits will be similar to those of plasma-arc-sprayed tungsten. Arc-sprayed W deposits are porous, possess a lamellar microstructure and low values of tensile strength (≈22 ksi). In contrast, sintering of the arc-sprayed material raises the density, produces equi-axed grains, and increases strength to ~70 ksi. The DBTT for arc-sprayed tungsten is also high (≈420°C). A further consideration is the

nature of the W substrate itself such as whether it is recrystallized or not. Differences in the morphology of the substrate and the deposit may also result in stress gradients.

4.2. Heat sink materials

Copper, zirconium, and vanadium alloys have been examined as potential heat sink materials. The requirements of these materials are the ability to withstand high heat fluxes, to withstand a modest level of radiation damage (10–20 dpa) and to be environmentally compatible with the surface materials and the coolant. The desirable properties of heat sink materials are a high thermal conductivity, a low coefficient of thermal expansion, resistance to fatigue failure, resistance to radiation damage and coolant corrosion, and good availability and fabricability.

4.2.1. Bulk properties

Several groups of copper alloys have been examined. They are pure copper, oxide-dispersion-strengthened copper alloys, low-concentration age-hardened alloys, and Cu-Be alloys. All these alloys have adequate thermal conductivity and low-temperature strength. Pure copper, however, loses its strength at relatively low temperatures. The oxide dispersion and age-hardened alloys present fabrication difficulties due to the importance of cold-work in achieving their mechanical strength. The bonding processes proposed (i.e. welding and brazing) require temperatures where the cold-work will be annealed out of the structure, and the strength will be significantly reduced. Only the Cu-Be alloys can achieve high strength without cold-working. The Cu alloys are available in a wide variety of forms, and they are easily fabricated. The evaluation of zirconium alloys has concentrated on the Zr-2.5Nb alloy which is used in the nuclear industry. The analysis of Valloys has concentrated on the V-15Cr-5Ti alloy which was developed for the fast breeder reactor programme. A comparison of the room-temperature properties of annealed oxygen-free copper; a Cu-Be alloy,(M25-1.8%Be, 0.2%Ni + Cr + Fe);Zr-2.5Nb; and V-15Cr-5Ti is shown in Table VII-8. The principle advantage of the Cu alloys is their high thermal conductivity. The V and Zr alloys exhibit a considerably lower thermal expansion coefficient than the Cu alloys, and the fatigue properties of the V alloys are considerably better than those of Cu alloys. For the conditions in INTOR, the limiter and divertor will be required to withstand a large number of cycles and, therefore, the fatigue properties will be an important factor in lifetime considerations.

TABLE VII-8. PROPERTY VALUES AT ROOM TEMPERATURE FOR CANDIDATE HEAT SINK MATERIALS

Property	OFHC copper (850°C annealed)	Zr-2.5Nb	Cu alloy M25	V-15Cr-5Ti
Thermal expansion ($\times 10^{-6}\cdot K^{-1}$)	16.5	6.3	16.5	9.3
Thermal conductivity ($W\cdot m^{-1}\cdot K^{-1}$)	336	26	105	21.3
Specific heat ($J\cdot kg^{-1}\ K^{-1}$)	390	300	420	451
Elastic modulus (GPa)	106	80	125	127
Electrical resistivity ($\mu\Omega\cdot cm$)	1.7	–	5.7	26
0.2% yield strength (MPa)	60	462	1085	490
Ultimate tensile strength (MPa)	200	593	1125	690
Elongation (%)	40	25	7	28
Fatigue limit (%) (at 10^8 cycles)	0.1	0.5 (est.)	0.3	0.7

4.2.2. Radiation effects

4.2.2.1. Copper

The swelling of pure copper, shown in Fig.VII-18, peaks at a temperature of ≈335°C. Upon extrapolation of these data, the swelling at fluence levels of 10^{26} neutrons$\cdot m^{-2}$ (30 dpa) ($E > 0.1$ MeV) is expected to be <0.01% if the material temperature is maintained below 235°C. However, the swelling of this material will increase to 9% if the material temperature is increased to 335°C. The swelling of copper can be reduced by use of fully cold-worked material, but partial annealing of the cold-worked material can result in increased swelling relative to the fully annealed material. The level of expected gaseous, i.e. oxygen and nitrogen, contamination of copper in the environment of a fusion energy device is not expected to increase the swelling. Moreover, the simultaneous implantation of helium and production of irradiation damage in copper from the deuterium-tritium fuel reaction is not expected to exacerbate the swelling that is obtained on neutron irradiation. The alloying of copper with either 1–3% aluminium, germanium, silicon, nickel, or beryllium can result in significant reduction of the void swelling.

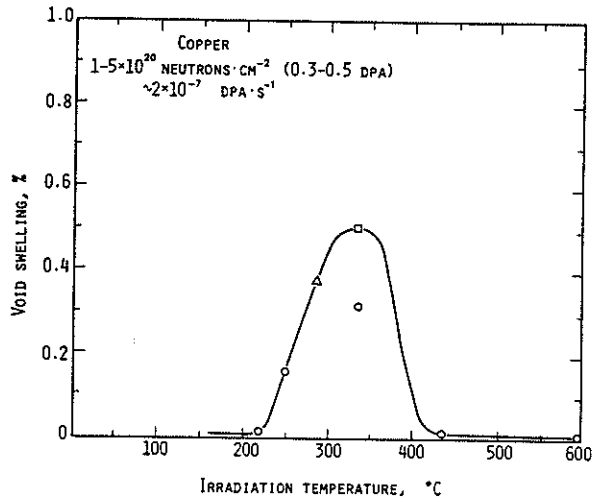

FIG. VII-18. Dependence of void swelling of neutron-irradiated copper on temperature.

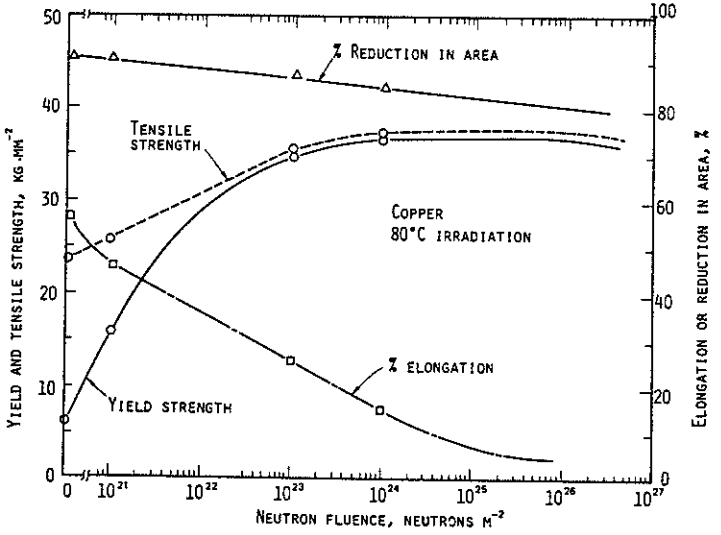

FIG. VII-19. Effect of irradiation at 80°C on room temperature tensile property of copper.

As shown in Fig. VII-19, the yield stress of copper is increased substantially with increasing neutron fluence up to $\approx 10^{23}$ neutrons·m^{-2}. The yield stress attains a nearly constant value (350 MPa) for fluence levels above 10^{23} neutrons·m^{-2}. The total elongation of copper is reduced from ≈28% to ≈7%, following exposure to a fluence of 10^{24} neutrons·m^{-2}. The reduction in area at fracture also tends to decrease with neutron irradiation but only by a small amount, i.e. 5% at 10^{24} neutrons·m^{-2}.

4.2.2.2. Vanadium

The swelling of the V-15Cr-5Ti alloy on neutron irradiation is expected to be very low (<0.01%) for material temperatures less than ≈800°C and for fluence levels less than $\approx 10^{27}$ neutrons·m^{-2} (≈60 dpa). The simultaneous implantation of helium and production of irradiation damage from the deuterium-tritium fuel reaction is not expected to exacerbate the swelling obtained on neutron irradiation. The dimensional stability (swelling) of the V-15Cr-5Ti alloy can be maintained during neutron irradiation by reducing the chromium and titanium content in the alloy and simultaneously maintaining the approximate chromium-to-titanium ratio.

The yield strength of the V-15Cr-5Ti alloy is increased substantially (500 to about 950 MPa) on neutron irradiation of 10^{25} neutrons·m^{-2} at 100°C. It is likely that this irradiation-induced increase of yield stress is a maximum value for still higher neutron fluence. The tensile elongation of the V-15Cr-5Ti alloy is reduced to ≈1.5% following neutron irradiation to 10^{25} neutrons·m^{-2} at 100 °C. This low value of elongation is characteristic of this alloy for a wide range of neutron fluence (10^{23} to 10^{27} neutrons·m^{-2}) because of its deformation behaviour. However, the elongation of the irradiated material during tensile deformation is expected to increase with increasing irradiation temperature above 400°C. Additional experimental data are needed to determine the effect of irradiation on the ductile-brittle transition temperature for the expected environment in INTOR.

4.2.2.3. Zirconium

The Zr-2.5Nb alloy exhibits strengthening and loss of ductility with irradiation as shown in Fig. VII-20 [14]. The radiation strengthening of Zr alloys is not completely understood, but it is believed that niobium acts to stabilize the radiation defects since radiation hardening is more pronounced in this alloy than in Zircaloy-2. Swelling has not been observed in Zr alloys tested in water-cooled fission reactors.

4.2.3. Corrosion/compatibility

Data on corrosion of the candidate heat sink materials are very limited under conditions projected for the limiter/divertor application. It is concluded, however,

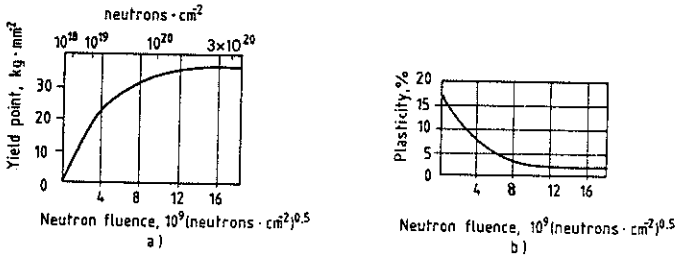

FIG. VII-20. Effect of irradiation of the yield point (a) and plasticity (b) of alloy Zr-2.5 Nb.

that corrosion of copper and copper-beryllium alloys should not be excessive at temperatures below 200°C if the water chemistry is controlled at reasonable impurity, e.g. oxygen, levels. Recent scoping studies conducted on corrosion of selected V alloys (V-15Cr-5Ti and V-15Cr) by water were very encouraging in that good corrosion resistance was observed at 250°C in de-oxygenated water [4]. Although alloys have generally not been recommended for use with water coolant, these data indicate acceptable corrosion resistance. Additional data should be obtained to confirm this conclusion. Zr alloys are successfully used in high-temperature pressurized-water conditions, and no extraordinary problems are anticipated for INTOR coolant conditions. Both vanadium and zirconium form hydrides at low temperatures, and thus hydrogen embrittlement is a concern. The solid solution solubility of hydrogen is much lower in zirconium so that hydrogen embrittlement could be more serious for Zr-2.5Nb.

4.2.4. Fabrication

Cu alloys are commercially available in a variety of shapes and sizes, and they generally exhibit good fabricability. Zr alloys are also commercially available. At present, V alloys are not available commercially. However, fabrication techniques for these materials were developed in the 1960s as part of the breeder reactor programme, and both forming and welding procedures have been established.

5. TILE ATTACHMENT CONCEPTS AND FABRICATION

5.1. Tile attachment concepts

A protective armour surface is required for the limiter blade, the divertor plates, and possibly for selected areas of the first wall. The main objectives of

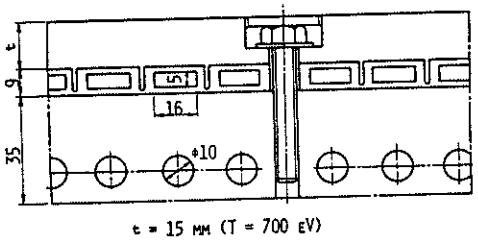

FIG. VII-21. Cross-section of mechanically attached limiter plate.

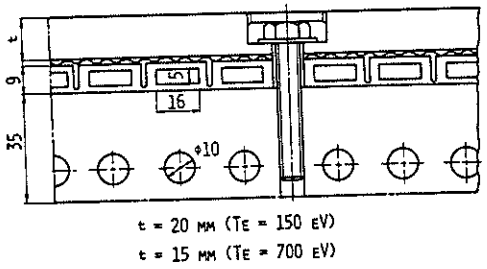

FIG. VII-22. Cross-section of mechanically attached limiter plate with rough surface plate to assure thermal conductance between the armour and heat sink.

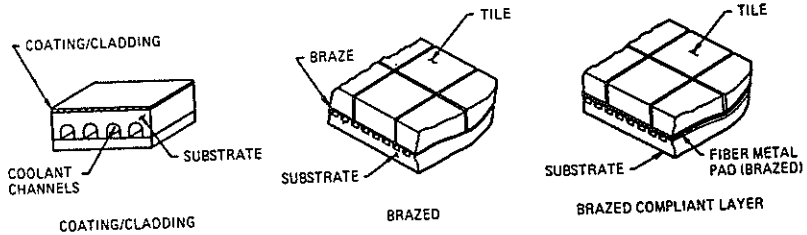

FIG. VII-23. Possible design concepts for conduction-cooled tiles.

any attachment concept are to maintain the materials in an acceptable temperature range and to minimize the thermal stresses through the structure. Various methods have been proposed to attach the armour surface to the actively cooled substrate. The different methods can be divided into three categories, which are illustrated in Figs VII-21 to VII-23:

(i) Radiation-cooled armour plate mechanically attached to the substrate;
(ii) Radiation-plus-conduction-cooled armour plate which can either be mechanically attached or bonded to an intermediate material between the armour and substrate;
(iii) Conduction-cooled armour plate which is metallurgically bonded to the substrate.

In general, radiation cooling results in the highest surface temperatures and the lowest thermal stresses, whereas the conduction-only concept results in the lowest surface temperatures but the highest thermal stresses.

5.1.1. Radiation-cooled concept

An illustration of a radiation-cooled armour is shown in Fig. VII-21, where a graphite tile is bolted to a stainless-steel heat sink. Each armour tile is attached to the stainless-steel plate by a tungsten bolt. This attachment is carried out in such a way that the thermal stress resulting from the difference of thermal expansion is reduced. The tungsten bolt is coated by ceramic material to protect the bolt from the reaction of tungsten and carbon to form tungsten carbide. In addition, the tungsten bolts are covered by the armour (C) material in order to protect them from plasma particles.

There are two concerns with the concept. First, the high temperature necessary for radiation cooling limits the possible armour materials to only very high-melting-point materials, such as C, W, Ta, or Mo. In the case of the graphite armour, the high temperatures result in excessive erosion by sublimation that leads to a shorter lifetime. Second, the mechanical attachment will require a non-usable tile thickness of about 1 cm to accommodate the bolt or attachment interface. The non-usable thickness results in a reduced erosion lifetime.

5.1.2. Radiation-plus-conduction-cooled concept

Examples of the radiation-plus-conduction-cooled concept are illustrated in Figs VII-22 and VII-23. This concept utilizes an interface layer between the armour and substrate which provides a moderate amount of thermal conductance but leads to moderate to low thermal stresses. The interface layer can be either mechanically attached or brazed. In the case of mechanical attachment, the surface of the interface layer is roughened so as to assure interface conductance. In the case of brazed attachment, a fiber metal compliant layer of known thermal conductance is used as the interface layer.

The major problems of this concept involve the interface layer. For the mechanical attachment, there is a concern that the thermal conductance may vary over time owing to irradiation swelling and creep. For the brazed concept, the irradiation response of the fiber metal is unknown, and high outgassing rates are possible in this material.

5.1.3. Conduction-cooled concept

The conduction-cooled concept is illustrated in Fig. VII-23. High thermal conductance is achieved by a metallurgical bond using techniques such as diffusion bonding, explosion bonding, plasma spraying, or brazing. The armour temperatures are kept low, but the thermal stresses are generally high. The major difficulty is that the allowable stress levels in the structure or the bond could be exceeded. There is also some concern about irradiation effects in the bond which have not been investigated so far.

5.2. Fabrication

All the concepts presented above appear fabricable with the technology available at present. However, development of the most appropriate techniques will be required. This section surveys the possible methods for bonding the surface armour to the heat sink.

5.2.1. Graphite

Joining techniques that may prove useful for the present application involve the use of brazing, graphite cements and diffusion bonding. Problems associated with the joining of graphite are generally similar to those arising for ceramic materials. The differences in coefficients of expansion between graphite and most metals are substantial. Also, graphite is not wet by conventional brazing alloys. The following graphite bonding methods were developed for nuclear applications. These methods may be applicable to the fabrication of a pumped limiter with a graphite armour. The brazing material is a Fe-Ni-Ti brazing alloy. This material has both good bondability to graphite and a small thermal expansion coefficient a elevated temperatures. This alloy can also be used in the very convenient form of a paste obtained by mixing pure metals in powdered form with an organic compound such as styrene as a binder. The advantage of this brazing paste is the ease with which any kind of composition can be prepared to suit a particular purpose, thus providing a very versatile brazing material. During the high-temperature brazing, the organic binder decomposes and vaporizes, leaving little residual carbon. Styrene is free of oxygen in its molecular structure, and thus cannot affect the bond of oxidation.

With the use of Fe-Ni-Ti brazing materials, the bonding of graphite to graphite can be carried out by different processes such as (1) high-frequency induction brazing, (2) inert-gas-shielded tungsten-arc ('tig') brazing, and (3) resistance brazing. The bonding of graphite to metal (titanium-copper) can also be carried out by high-frequency induction brazing. The optimum brazing temperatures are 1200 to 1400°C for the graphite-titanium joint formed by this process. After joining graphite to titanium, the bonding of titanium to copper can be made by a conventional brazing method.

Graphite cement is the most widely used method for joining graphite and is recommended for use here. The cements are heavily loaded suspensions of fine graphite powder in a resin binder. The strength and thermal conductivity of cemented joints are inferior to the properties of bulk graphite. Typically, these joints have low ductility, and the radiation response has not been determined.

Only limited research has been conducted on diffusion bonding of graphite Most of the work is on bonding of graphite to graphite. Considerable development is required before diffusion bonding of graphite to metals could be recommended.

5.2.2. Silicon carbide

A new brazing technique of SiC to SiC has been developed. This technique uses mixtures of a halogen chemical compound and kaolin as the component of adhesion. SiC-SiC, with the mixtures for adhesion between them, are bonded by heating in the air at a temperature above 1300°C. The highest tensile strength is 70 MPa.

Another brazing method of SiC to copper or aluminium is being developed. SiC (10 mm thick) and copper (0.1 mm thick) with a Cu-Mn alloy (50 μm thick) between them are bonded by heating in an argon gas atmosphere. The brazing temperature is above 860°C (melting point of the Cu-Mn alloy). When the thickness of either the SiC or metallic substrate is sufficiently small, the results are satisfactory. Using the same technique, SiC (~10 mm) is also successfully brazed onto aluminium (~10 mm). There still remain some problems with the large differences in thermal expansion between SiC and copper or aluminium. Experiments testing the bond resistance against cyclic thermal stress are underway.

Metallization currently appears to be the preferred method of bonding SiC to a metal substrate. In the most widely used metallization technique, i.e. the moly-manganese process, a mixture of metal and metal oxide powders suspended in nitrocellulose lacquer is painted onto the ceramic surface and fired in a wet H_2–N_2 atmosphere typically at 1400°C. Because of this high metallization temperature, a thick fiber metallization with the Ti-Mo process is suggested for bonding the SiC and then hydrogen-brazing the metallized surface to the substrate with a Ni-Cu-Ag braze. The metallization bond is typically quite strong (about 35–70 MPa) but quite brittle.

5.2.3. Beryllium

Bonding of beryllium to the metallic substrate appears feasible by plasma spray, brazing, diffusion bonding and electron beam welding. The plasma spray process, which has several advantages, is the preferred method of fabricating duplex limiter/divertor walls with beryllium. Centimetre-thick coatings of beryllium can be sprayed onto parts of relatively complex shape.

Beryllium and copper are bonded easily by the diffusion bonding at temperatures of 800 to 900°C. Electron beam welding is also available for the bonding of beryllium to copper. Vacuum or inert-gas atmospheres are generally needed in the bonding of beryllium because of its high chemical affinity for oxygen.

5.2.4. Beryllium oxide

Although there is limited experience with bonding of beryllium oxide, probably much of the experience gained with bonding other oxides is applicable to this case. In general, the methods considered for SiC are probably also applicable to BeO. The dual metallization/brazing process appears to offer the best solution. Most of the experience with metallization is for bonding oxides such as Al_2O_3. Silver, copper, and Ag-Cu brazes are most frequently used to braze metallized ceramics to metals. Further development is recommended for the bonding of BeO to the candidate substrates.

5.2.5. Tungsten

Brazing, plasma arc spraying and chemical vapour deposition are candidates for the duplex attachments. Direct bonding techniques such as melting copper onto tungsten, diffusion bonding and explosive bonding are also considered. Brazing is recommended over plasma arc spraying or CVD. Though machining and brazing of pure tungsten are relatively difficult, the rich W alloy called Heavy Alloy is a promising material. This alloy, which consists of tungsten (9)-96 wt-% and copper or nickel, permits machining and brazing. A tungsten alloy called Elconite, whose content of added metals such as copper and silver is richer than that of Heavy Alloy is also a possible candidate. Its brazing and machining properties are reliable, and its thermal expansion coefficient is larger than that of Heavy Alloy. A thin layer of Elconite, inserted between the heat sink and the armour made of tungsten, will reduce the thermal stresses since the thermal expansion coefficient of this alloy is intermediate between pure tungsten and copper.

Tests on joints between tungsten and copper obtained by pouring copper on Ni-plated tungsten have shown high resistance under cyclic loading. The surface of a tungsten disc brazed by this method to a watercooled copper block has

been cycled between 420°C and 250°C. The braze remained intact for more than 10 000 cycles.

5.2.6. *Tantalum*

For tantalum coatings on the heat sink materials of interest here, the direct bonding processes – either diffusion bonding or explosive bonding – appear to be the most attractive. Although Ta-V alloy composites have not been produced or evaluated, there appears to be little reason for expecting that these combinations would not be compatible. Since the metallurgy of these two refractory metals is generally very similar, this combination probably represents a better matching of physical, mechanical and chemical properties than Ta-Cu.

Tantalum has been diffusion-bonded with considerable success to both copper and stainless steels. The bi-metal cladding produced was a 1.5-mm layer of tantalum on a 6.3-mm Cu base. Diffusion-controlled bonding was performed in vacuum to minimize contamination. Tantalum has been explosively bonded to a variety of materials including stainless steels and copper. Parts as large as 1 m X 3 m are routinely produced. These claddings are generally only a few millimetres thick but direct contact with vendors indicates that unalloyed tantalum could be explosively bonded in thicknesses up to 2 or 3 cm without difficulty.

6. THERMAL HYDRAULIC AND STRESS ANALYSIS

The successful operation of the impurity control system depends to a large degree on the thermal and stress behaviour of the components. During Phase Two A, the thermal and stress response of the pumped limiter was explored in detail, and this section summarizes the results of the analyses for various limiter designs. The results presented here are for the reference limiter configuration of a curved, double-edged limiter which is cooled by low-temperature water (≈100°C). Two heat load conditions are considered: 2–3 $MW \cdot m^{-2}$ corresponding to the medium and high edge temperature conditions, and a 1.3 $MW \cdot m^{-2}$ peak loading corresponding to the low-edge-temperature condition. In addition, a flat limiter was analysed, and detailed parametric analyses were conducted. Details concerning this additional work can be found in Refs [1–4]. It should be noted that the limiter operating conditions are similar to the divertor operating conditions so that the thermal and stress results can generally be applied to the collector plate as well.

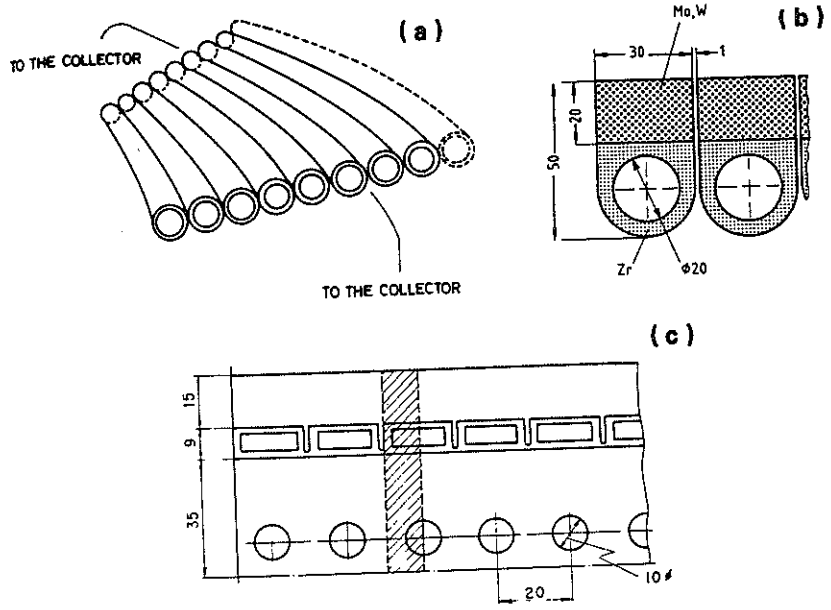

FIG. VII-24. Limiter designs considered for thermal and stress analysis:
(a) tube array used at low edge temperatures;
(b) tube-like array with protective surface layer;
(c) plate structure (cross-hatching area considered for thermal and stress analysis).

6.1. Limiter design description

Several limiter designs have been considered, as is shown in Fig. VII-24. Conceptually, the simplest design consists of an array of tubes, each of which is 25 mm in diameter and has a wall thickness of 2.0 mm (Fig. VII-24a) [1]. The tube design has been considered for use at the low edge temperature where sputtering erosion is insignificant for medium- and high-Z materials and where the heat load is low. Under these conditions, stainless steel can be used as the tube material. The peak heat load to the tubes is only 1.3 $MW \cdot m^{-2}$. The next design also makes use of a tube-like arrangement, but a thick surface layer is provided on the side exposed to the plasma (Fig. VII-24b) [3]. The thick layer is necessary to allow for erosion that takes place during operation. The width of each piece is 30 mm, the inner diameter of the tube is 10 mm, and the thickness of the surface layer is 20 mm. Molybdenum and tungsten are considered as surface materials,

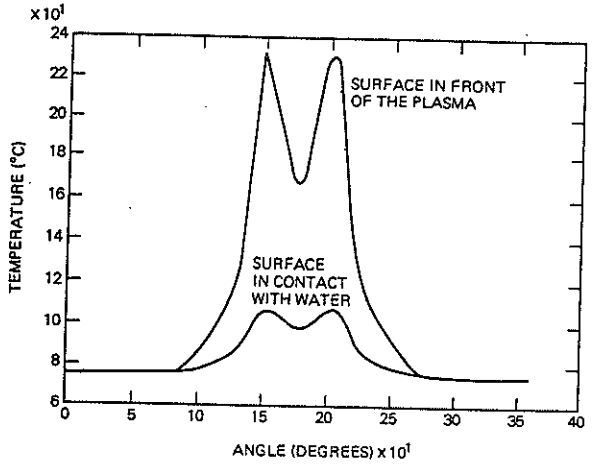

FIG. VII-25. Inner and outer temperature of central tube of the tube array (for low plasma edge temperature).

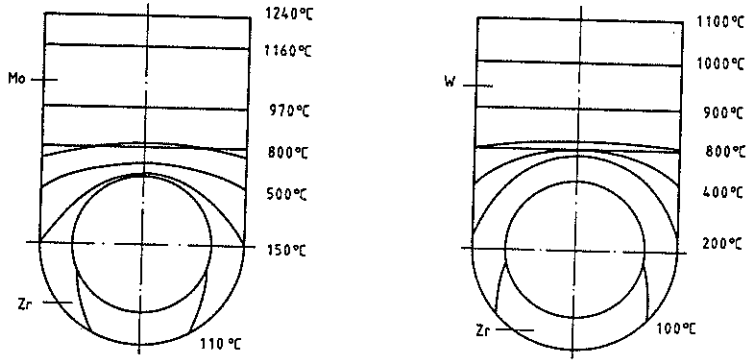

FIG. VII-26. The temperature distribution for the composite tubular design for the limiter ($q = 2\ MW \cdot m^{-2}$).

and zirconium is proposed as the tube material. This design is also limited to low edge temperatures because of the self-sputtering restrictions of high-Z materials. If the molybdenum or tungsten were replaced by a low-Z material, then this design would be applicable to medium and high edge temperatures. The heat load to the surface has been assumed to be 2 $MW \cdot m^{-2}$. The other type

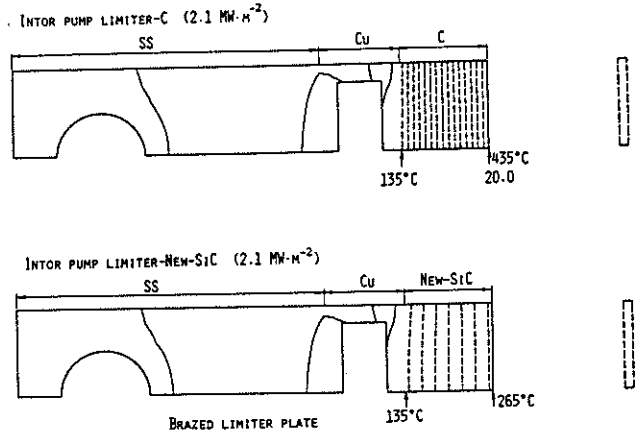

FIG. VII-27. Temperature profile of C, new-SiC armour at top surface limiter plate for $q = 2.1\ MW \cdot m^{-2}$ (unirradiated).

of limiter configuration is a plate composed of stainless steel and copper with machined coolant channels [2]. Surface tiles are metallurgically bonded to the copper (Fig. VII-24c). This plate-type design is considered to be the reference design for the INTOR limiter. Several materials have been considered, but the results shown here are for carbon and SiC with a surface heat flux of 2 $MW \cdot m^{-2}$. A similar plate design has also examined beryllium as the surface material for a surface heat flux of 2.4 $MW \cdot m^{-2}$ [4].

6.2. Limiter temperature distribution

The calculated temperatures in the three limiter designs for thermal-equilibrium conditions during the plasma burn are shown in Figs. VII-25 to VII-27. The temperatures in the stainless-steel tube located at the centre of the tube array vary significantly with angular position, as is shown in Fig. VII-25 (the top surface of the tube is located at 180°). The variation is caused by the changing heat flux that occurs as the angle between the magnetic field lines and the tube surface changes around the circumference. The peak temperature of ≈240°C is well within allowable temperature limits. The temperature distribution through the tube-like structure with protective tiles of molybdenum or tungsten are shown in Fig. VII-26. The peak temperatures are 1240°C and 1100°C for molybdenum and tungsten respectively. Although the temperatures are high they are within acceptable limits for these high-melting-point metals. The increased temperatures

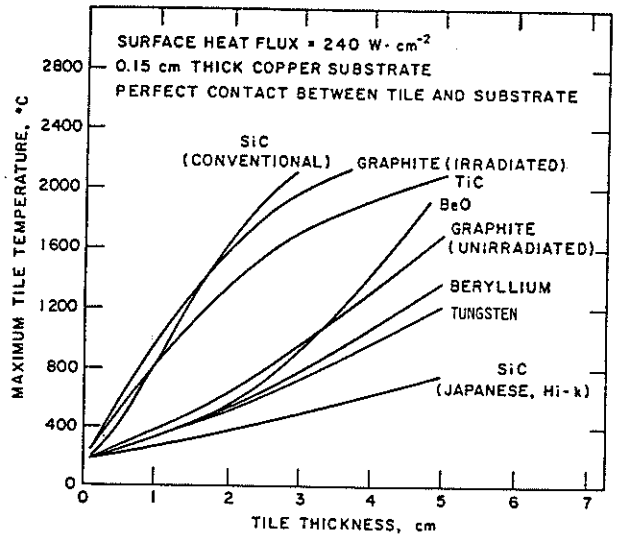

FIG. VII-28. Maximum tile temperature versus thickness for limiter/divertor (perfect contact).

compared with the tube array are due to the higher heat flux and the thicker structure. The temperature distributions through the plate limiter are shown in Fig. VII-27 for graphite and high-thermal-conductivity SiC. Again the peak surface temperatures are low. Similar temperatures are calculated for a plate limiter with beryllium as the plasma-side material.

The surface temperatures in the material exposed to the plasma depend upon the type and thickness of the material. The variation in surface temperatures as a function of thickness is shown in Fig. VII-28 for several candidate tile materials on a plate limiter. The temperatures are dependent on the thermal conductivity of the materials, with low-conductivity SiC exhibiting the highest temperatures. Also illustrated is the effect of irradiation on the temperatures in graphite. Irradiation decreases the conductivity of graphite, and hence the temperatures are increased. Similar effects of irradiation on conductivity are likely in other non-metals such as SiC and BeO.

6.3. Stress analysis

Stress restrictions will limit the heat fluxes and thicknesses permitted for the limiter. The calculation of stresses and their effect on operation is generally

more involved than the calculation of temperatures. The additional complexity is due to the additional information necessary for a complete stress analysis and the larger number of properties that need to be evaluated. Additional information, such as how the limiter sections are attached to each other and to the first wall/blanket, the sizes of the tiles, the bonding procedure and the presence of flaws or cracks, is important for a thorough stress evaluation. The properties of greatest interest are the mechanical properties (strength, ductility, creep, fatigue and crack growth) and the physical properties (thermal expansion, elastic modules, Poisson's ratio). It is also desirable to include the effects of irradiation on these properties in the stress analysis. Another important consideration in the stress analysis is the criteria that are used to judge the acceptability of a particular design. At present, there is no generally accepted fusion stress criteria code, and therefore available codes such as the ASME Code, Section 3, Case N 47 for Class I components, are utilized to determine acceptable stress levels.

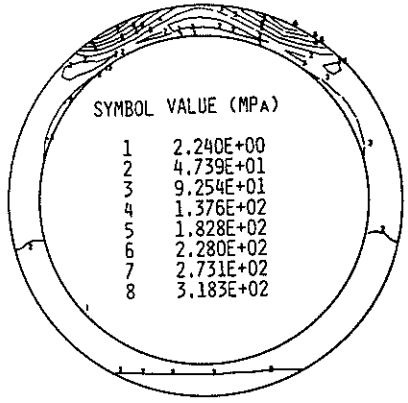

FIG. VII-29. Von Mises stress contour plot for central tube.

Stress estimates have been made for the three limiter designs. The Von Mises stress contours for the central tube of the tube array are shown in Fig. VII-29. The stresses are peaked in the areas where the temperatures are the highest. The peak Von Mises stress level of 318 MPa is below the peak allowable stress for cold-worked austenitic stainless steel. The stress fields for the composite tube limiter design are illustrated in Fig. VII-30. The fact that two different materials are metallurgically bonded together results in significant thermal stresses across the

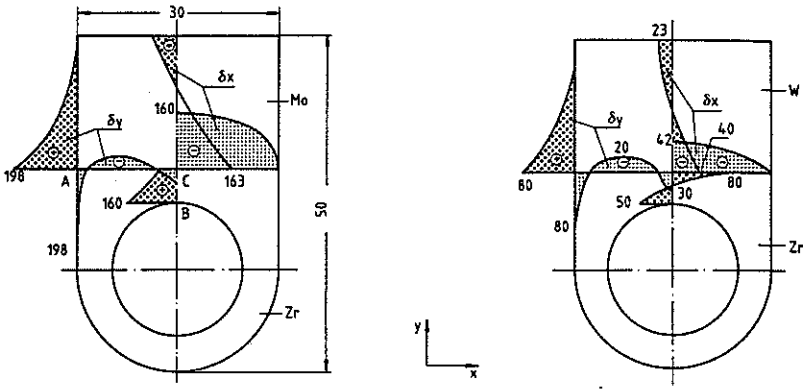

FIG. VII-30. The fields of stresses in typical cross-sections of the composite tubular design of limiter ($q = 2\ MW \cdot m^{-2}$, stress levels are in MPa).

interface. The interface stresses are caused by the mismatch in the thermal expansion coefficients of the two materials. The calculated stresses are again within acceptable limits. The stresses in the plate limiter are shown in Fig. VII-31. The stress levels in copper and stainless steel are quite low (about 45 MPa) for the graphite tile design, but the stresses in copper are much higher (138 MPa) for the SiC design. The reason for the low stresses with graphite is the very low elastic modulus in graphite which limits the graphite stress to only 17 MPa. The stresses in copper for the SiC design are slightly above the ASME allowable stress of 117 MPa for annealed OFHC copper.

Maximum stresses in the heat sink have been determined for a plate limiter with Be as the plasma-side material, as shown in Table VII-9. Three heat sink materials and two stress constraints were considered. One conclusion of these calculations is that annealed copper is unacceptable because the thermal stresses exceed the ASME allowable stress of 117 MPa. However, a high strength copper alloy, like Cu-2Be, and V-15Cr-5Ti, is acceptable from this standpoint. Other conclusions are that tile constraint generally imposes stresses in the top surface of the heat sink higher than without tile constraint, and that the different geometry at the leading edge along with the lower surface heat flux results in significantly different stresses.

An analysis of fatigue lifetime has been conducted to estimate the allowable number of operating cycles for a plate limiter as a function of tile thickness. ASME safety factors of a factor of two in strain range or a factor of 20 in cycles to failure whichever is lower, were employed in the analysis. The major conclusion of the analysis is that a Cu substrate can operate for about 10^4 cycles with a tile

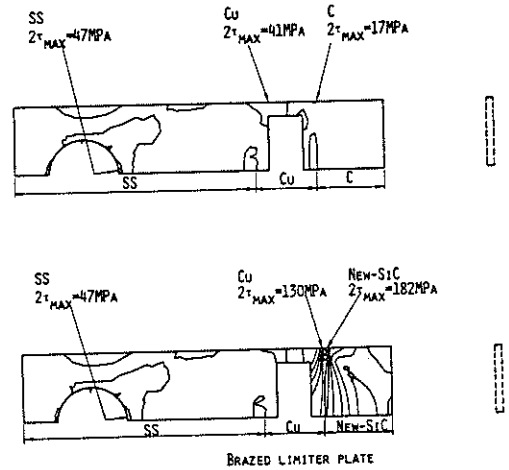

FIG. VII-31. Stress distribution in C, new-SiC (BeO-rich) armour at top surface limiter plate (heat flux 2.1 $MW \cdot m^{-2}$) (unirradiated).

thickness of 10 mm. The number of cycles to failure is reduced to about 10^3 cycles for a tile thickness of 30 mm. Increased fatigue lifetime is possible with a V alloy structure since this material has superior fatigue properties to copper.

6.4. Conclusions

The thermal hydraulic and stress analyses indicate that acceptable temperatures and stresses are achievable for several possible limiter designs. Additional optimization studies are needed to examine composite designs. Areas of future work should include examinations of tile size effects, fabrication effects, bond failure, crack growth behaviour, and the influence of irradiation.

7. ELECTROMAGNETICS

7.1. Introduction

As the plasma current decays during a plasma disruption, currents and voltages are induced in the first wall and impurity control systems. These currents can interact with the magnetic field to produce large forces and torques. The induced voltages can also lead to arcing between segments of the

TABLE VII-9. CALCULATED STRESS IN LIMITER STRUCTURAL MATERIAL

Structural material	Be coating thickness (mm)	Max. stress range (MPa) Top surface (2.4 MW·m^{-2})	Leading edge (1 MW·m^{-2})	$3S_m$ (MPa)
Annealed Cu[a]	1	154	93	120
	10	158	218	120
	20	161	246	120
	30	165	330	120
Cu-2Be (M-25)[a]	1	154	93	1225
	10	158	218	1225
	20	161	246	1225
	30	165	330	1225
V-15Cr-5Ti[b]	1	241	152	560
	10	471	253	560
	20	501	292	560
	30	528	305	560

[a] No tile constraint.
[b] With tile (2 cm wide) constraint on structure.

limiter or divertor. During Phase Two A analyses were conducted to estimate the magnitude of the forces. Three of the participants conducted analyses without taking account of shell effect of first wall [1–3]. A more detailed analysis, which included the effect of a conducting first wall, was also performed by one of the participants [4].

The evaluation of the currents, voltages, and forces in the first wall and limiter is generally a complicated undertaking. The analyses performed in Phase Two A have made rough estimates of these quantities, but exact calculations require an extensive effort that is beyond the scope of this project.

7.2. Analysis without conducting-shell effect

Eddy currents are induced in the pumped limiter during a plasma disruption. An electromagnetic force due to the interaction between the eddy current, I, and

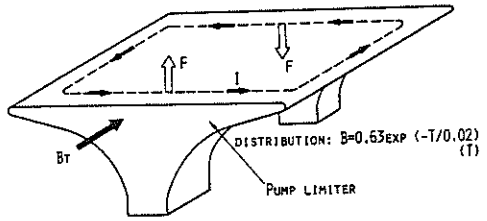

FIG. VII-32. Electromagnetic force on the pumped limiter.

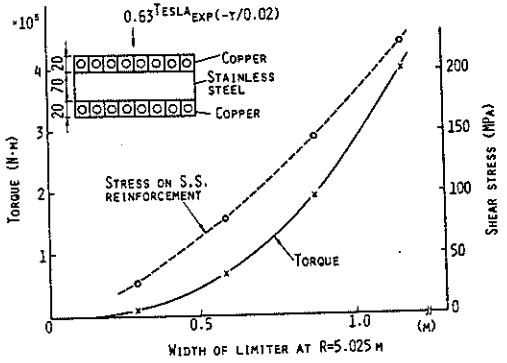

FIG. VII-33. Torques and stresses versus limiter width.

toroidal magnetic field, B_T, is shown conceptually in Fig. VII-32. This electromagnetic force causes torsion to the limiter. The eddy current distribution on the limiter plate is estimated from the magnetic flux change distribution on the plate which is obtained by assuming that the line plasma current decays with a 20 ms time constant. Type 316 stainless steel is used for the reinforcement against the torques induced by the electromagnetic force in the pumped limiter. To reduce the force in the Cu cooling plate as much as possible, grooves are cut nearly up to the rear side of the Cu plate. Torques around the radial centre line of the plate and stresses in the stainless-steel reinforcement for the double-edged limiter are shown in Fig. VII-33 as a function of the limiter width. The joint between the Cu plate and the reinforcement is subjected to about the same shear stress as appears on the reinforcement. The allowable stress is $0.8S_m$ (Cu: $0.8S_m = 31$ MPa, stainless steel: $0.8S_m = 108$ MPa, according to the ASME

code, Section 3. To make the shear stress lower than the allowable stress for copper, the width of the plate and torque should be less than 340 mm at R = 5 m and 2×10^4 N·m, respectively.

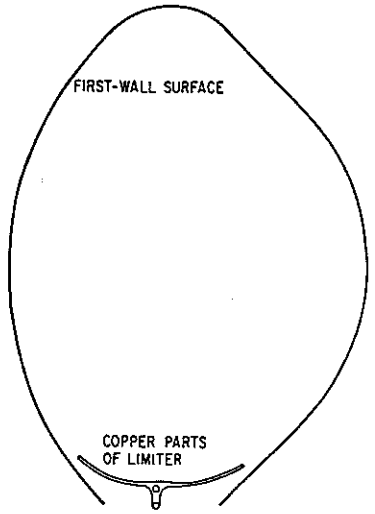

FIG. VII-34. Configuration of first wall and limiter used for calculation.

7.3. Analysis with conducting first wall

The influence of a conducting first wall on the forces in the limiter was examined by using a computer code that was developed to model the induced currents in the first wall and limiter as a function of time. The configuration used in the analysis is shown in Fig. VII-34. The first wall and limiter were modelled as a series of co-axial circular wires whose positions and conductances approximated the overall electrical configuration of the system. The plasma is modelled as a single current loop. During a disruption, the plasma current decays, inducing currents in the co-axial wires. The segmentation of the toroidal limiter has been modelled by considering a single cut in the limiter in the radial direction. The cut is modelled by imposing an additional voltage term on the limiter wires only. The voltage is made large enough to make the sum of the limiter currents vanish. Resistive voltages near the cut due to radial flow are neglected.

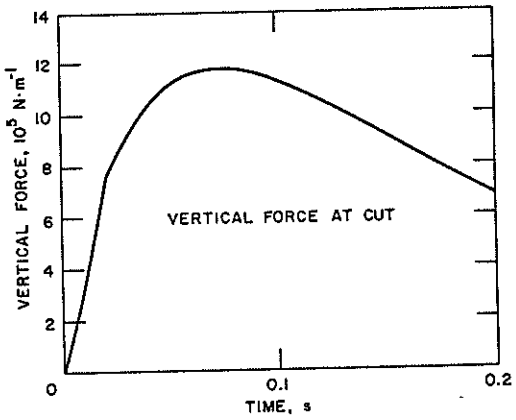

FIG. VII.35. Induced vertical force at single poloidal cut, for a first-wall time constant of 100 ms.

The largest forces induced during a disruption involve the interaction of the radial currents at the single cut and the toroidal magnetic field. The force of interaction between the toroidal magnetic field and the radial currents at the cut is reduced by the conducting first wall. With a non-conducting first wall, the force peaks at 20 ms, the end of the plasma current disruption. At that time the vertical force on each side of the cut is 3.50 MN. The conducting first wall reduces the currents in the limiter, and reduces the force at 20 ms to 0.78 MN. However, as the current in the first wall decays, with a 100 ms time constant, the current in the limiter is driven higher; the vertical force on each side of the cut peaks at 75 ms, at a value of 1.18 MN. The time variation is shown in Fig. VII-35.

The effects of multiple segmentation cannot be calculated with the co-axial ring model. It is, however, possible to give a physical argument to estimate the forces on a segmented limiter on the basis of the forces on a limiter with a single cut and the increased resistance of current paths in a segmented limiter.

The resistance of the radial current path at the cut is neglected in the above calculations with a single cut, surely a good approximation because the radial width of the limiter is small relative to its circumferential length. If the number of segments is increased until the radial width and length are equal (about 24 segments), the resistances of the radial and azimuthal paths are equal and the current is roughly halved. If the number of segments is further increased, the resistance of the radial current paths becomes dominant, and the current varies inversely with the number of segments. For 72 segments, six per TF coil, the current and vertical force should have one third of their value with 24 segments.

TABLE VII-10. INTERACTION BETWEEN LIMITER EDGE CURRENTS AND TOROIDAL MAGNETIC FIELD

First-wall time constant (ms)	0	100	100
Time (ms)	20	20	75
Vertical force with one cut: computed (MN)	3.50	0.78	1.18
Vertical force with 24 cuts: estimated (MN)	1.75	0.59	
Vertical force with 72 cuts: estimated (MN)	0.88	0.30	

To be conservative, the value of one half was used. These values appear in Table VII-10. Support against a force of 0.30 MN, with its resulting torque about a radial axis, is believed to be manageable.

7.3.1. Variation of force with first-wall time constant

A series of computations was performed for a Cu ($\rho = 0.017\ \mu\Omega\cdot$m) limiter with a single poloidal cut. Time constants of t = 0, 10, 30, 100, and 1000 ms were used. The resulting peak values of F_R, F_Z, N, and F_{cut} are shown in Fig. VII-36. F_R is the radial force per unit length of limiter due to the interaction of the induced toroidal current with the vertical component of poloidal field. F_Z is the vertical force per unit length of limiter due to interaction of the induced toroidal current with the radial component of the poloidal field. The poloidal field is the sum of the fields from the PF coils, the plasma current, and the induced currents themselves. N is the torque per unit length of limiter, about an axis in the toroidal direction, resulting from F_R and F_Z. F_{cut} is the vertical force of interaction between the toroidal field and the radial currents which flow wherever the limiter has a poloidal cut.

The dashed straight line in Fig. VII-36 shows the slope for a hypothetical force which varies inversely with the square root of τ. The three quantities F_R, N, and F_{cut} have roughly the same behaviour. For $\tau \ll 20$ ms, the plasma current decay time, the force is largely independent of τ. The decrease of force with increasing τ is strongest for $\tau \approx 20$ ms. Finally, for $\tau \gg 20$ ms, the force decreases more evenly with increasing τ. The values of F_{cut} were divided by ten to fit them onto the same graph.

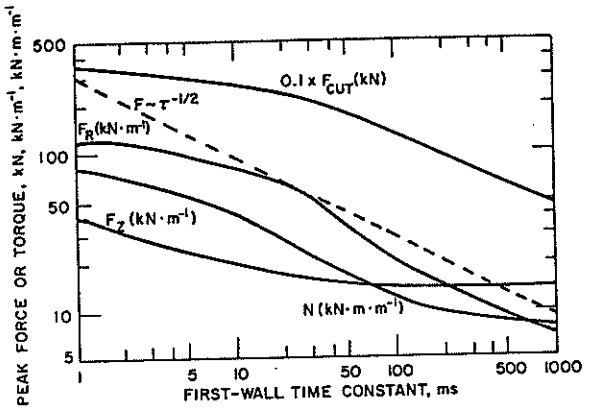

FIG. VII-36. Variation of forces and torque on limiter with time constant of first wall.

7.3.2. Variation of force with limiter resistivity

These computations were performed for a limiter with a single cut and a first-wall time constant of 100 ms. The three computations differed only in limiter resistivity: values of $\rho = 0.017$ (Cu), 0.07 (Cu-2Be), and 0.32 (V-15Cr-5Ti) $\mu\Omega\cdot$m were used. The resulting peak values of F_R, F_Z, N, and F_{cut} are shown in Fig. VII-37.

All four curves show roughly the slope of the dashed line, which represents a hypothetical force varying inversely as the square root of the resistivity. The values of N have been divided by ten, and those of F_{cut} by 1000, so that all forces could appear in the same graph but have no overlap to a confusing degree.

7.4. Induced voltages between limiter segments

Concern has been expressed that the voltage induced by plasma disruptions may lead to arcing between limiter segments. There is considerable uncertainty about how large the voltage between segments can be and still avoid damage from arcing, with values between 20 and 200 V suggested. It is prudent to use the 20 V value if possible.

In the computations for a limiter with a single cut, the zero net current condition is imposed by finding the electrical potential which reduces the circulating current to zero. For a limiter with a single cut, this potential represents the voltage across the cut. For a limiter with n segments and n cuts, the voltage across each cut is given approximately by dividing the potential by n.

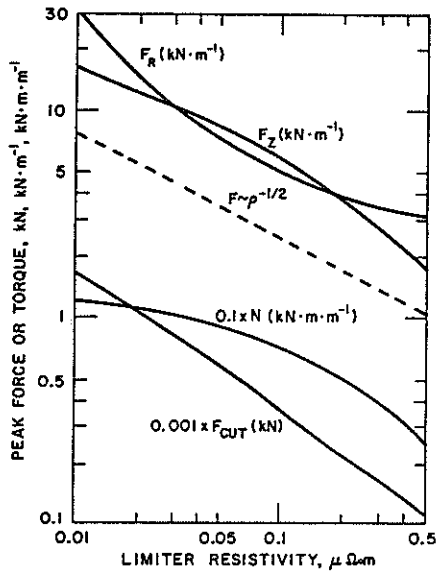

FIG. VII-37. Variation of forces and torque on the limiter with limiter resistivity.

For a first-wall time constant of 100 ms, the voltage across a single cut is calculated to be 450 V or 6.2 V per segment, for 72 segments. The voltage drop is predicted to be virtually independent of the limiter resistivity.

Conclusions

Several conclusions can be drawn from these studies:

(1) The electromagnetic force and torque around the radial centre line of a limiter segment are manageable when the limiter is segmented into more than ten pieces;
(2) The electrical response of the limiter is sensitive to the electrical behaviour of the first wall. Analysis without conducting-first-wall effect gives the maximum electromagnetic force;
(3) There is a characteristic variation of limiter forces and voltage with the first-wall time constant τ, with virtual independence of τ when τ is small compared with the plasma current decay time constant $\tau_0 = 20$ ms, rapid decrease with increasing τ when $\tau \approx \tau_0$, and inverse square root decrease with τ when $\tau \gg \tau_0$;
(4) Induced forces and torques vary inversely with the square root of the limiter resistivity; voltages are virtually independent of the limiter resistivity.
(5) For a first-wall time constant of 100 ms and a limiter segmented into 72 pieces, voltages between adjacent segments are manageable.
(6) In the light of the importance of conducting-first-wall and segmentation effects, further analysis in this area is required.

8. DISRUPTIONS

Disruptions can potentially limit the life of the limiter, divertor and first wall. The surfaces of these components are subject to melting and/or vaporization during disruptions. In addition, induced currents will result in forces within the melt layer leading to material losses from the surface. In this section, the thermal response of candidate surface materials and the stability of the melt layer are discussed.

8.1. Disruption scenario

Reference disruption conditions for the limiter, divertor, and first wall have been established. Both major and minor disruptions have been considered. The primary disruption parameters are the energy deposition per unit area, the disruption time, and the frequency of disruptions. A summary of the different cases is shown in Tables VII-1 and VII-2. The reference thermal quench time is 20 ms with 5 ms as the alternate time. The reference energy loads during major disruptions are 230 J·cm^{-2} for the divertor (case 1) and 270 J·cm^{-2} for the limiter (case 3) with 535 J·cm^{-2} as an alternative high-energy load to the limiter (case 2). Corresponding to these cases 1 to 3, the energy loads to first wall are 175 J·cm^{-2}, 35 J·cm^{-2} and 175 J·cm^{-2}, respectively. The reference energy load during minor disruption is 170 J·cm^{-2} for both of divertor and limiter.

It should be emphasized that there are considerable uncertainties in the disruption scenario. The energy densities and disruption times are not well characterized from present experiments, and therefore a large extrapolation is required to estimate the INTOR conditions. Also, the disruption frequency can be expected to vary from the estimates shown in Table VII-1. Because of these uncertainties, the INTOR participants have examined the materials response to disruption over a wide range of energy densities. The information presented here is generally for the reference conditions. Additional details concerning disruptions are presented in Refs [1–4].

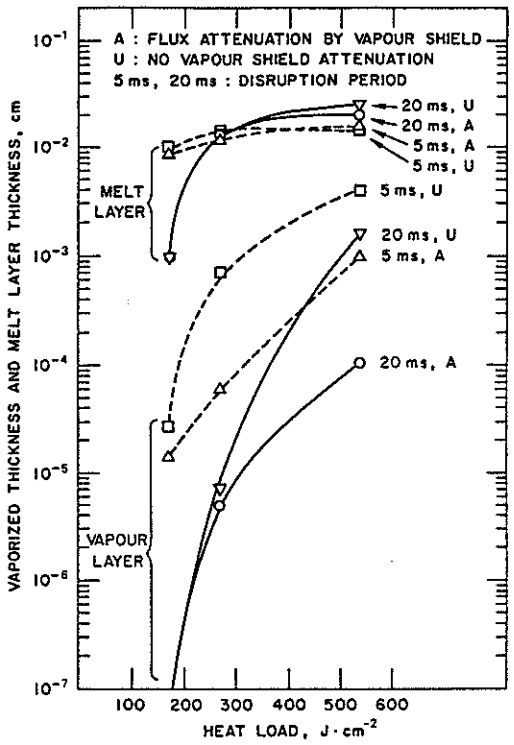

FIG. VII.38. Vaporized thickness and melt layer thickness of stainless steel.

8.2. Thermal response

The vaporization and melting characteristics of surface materials to a particular set of disruption conditions depend upon the thermo-physical properties such as thermal conductivity, specific heat, heat of fusion, heat of vaporization, melting point, and vapour pressure. The amount of vaporization and melting is also dependent on the initial temperature of the surface material. A high initial temperature relative to the melting point will lead to larger vaporization and melt layer thicknesses. In general, materials with low melting points and high thermal conductivities are expected to exhibit the greatest melt layer thicknesses. Another important aspect of materials response is the effect of a vapour cloud on the amount of energy deposited on the surface. As vaporized material is formed

during a disruption, a portion of the energy in the disrupting plasma is lost to the vapour cloud, and the amount of energy reaching the material surface is reduced.

A large number of candidate surface materials have been analysed by the INTOR participants. The materials considered are C, Be, BeO, SiC, TiC, W, Mo, and austenitic stainless steel. The reduction in wall thickness is taken into consideration in the numerical transient calculations by applying a moving-boundary condition. The energy flux attenuation by vapour shielding and recondensation of the vapour to the surface are also taken into account [4]. The analysis includes cases with and without the effects of vapour shielding. An example of the melt layer and vaporization thicknesses predicted for stainless steel is shown in Fig. VII-38, and a summary of the results for all materials is listed in Tables VII-11 to VII-14.

Several generalizations can be made from Fig. VII-38. First, there is a threshold energy below which no melting or vaporization occurs. For a 20 ms disruption time this energy is about 170 $J \cdot cm^{-2}$ in the case of stainless steel. Second, above this energy level, the melt layer thickness increases rapidly and then begins to level off. For stainless steel, the peak melt layer thickness is 100 to 200 μm. The vaporization thickness continues to increase as the energy density increases. Third, the effect of the vapour shield is to reduce the total melt layer and vaporization thicknesses. The relative reduction is greatest near the threshold energy. Notice that the rapid increase in the melt layer thickness for energy densities greater than the reference value of 170 $J \cdot cm^{-2}$ is an important source of uncertainty.

Tables VII-11 to VII-14 indicate that there are large differences in disruption response by the different materials. Stainless steel and beryllium show the largest melt layer thicknesses over the entire range of parameters that were considered. For the reference first-wall conditions (175 $J \cdot cm^{-2}$, 20 ms), the melt layer for stainless steel is predicted to be in the range of 7 to 24 μm, and no melting is predicted for beryllium. (The ranges indicated in the tables bracket the the values predicted by the INTOR participants.) When either stainless steel or beryllium is used on the limiter, the melt layer thickness is predicted to be large. For the reference limiter conditions (270 $J \cdot cm^{-2}$, 20 ms), the melt layer for stainless steel is predicted to be 120–150 μm, and the melt layer for beryllium is predicted to be 40–140 μm. Vapour shielding is calculated to reduce the melt layer thicknesses, but by less than a factor of two. The formation of a thick melt layer and the possible loss of material will have a large effect on the lifetime as was discussed in Section 10. The high-melting-point metals, W, Ta, and Mo, are not expected to melt or vaporize for the reference conditions at the first wall, limiter or divertor. Two non-metals, C and SiC, do not melt, and therefore they appear to be particularly attractive with respect to material losses by disruptions. Graphite also exhibits very low vaporization losses due to its high sublimation temperature. Vapour shielding is predicted to reduce the vaporization thicknesses

TABLE VII-11. MAJOR DISRUPTIONS – CASE 1: DIVERTOR CASE

	Material	Disruption Period (ms)	Disruption Model[a]	Melt layer thickness (microns)[b]	Vaporized depth (microns)
First wall ($170\ J \cdot cm^{-2}$)	Stainless steel	5	A	60 ~ 90	0.1 ~ 0.32
			U	90 ~ 110	0.38 ~ 2.8
		20	A	7 ~ 24	$<10^{-2}$
			U	7 ~ 24	$<10^{-2}$
	Beryllium (initial temp. 300°C)	5	A	60	0.2
			U	80	1.0
		20	A	NM	–
			U	NM	–
	Tungsten	5	A	NM	–
			U	NM	–
		20	A	NM	–
			U	NM	–
	Graphite	5	A	–	<1.0
			U	–	<1.0
		20	A	–	<1.0
			U	–	<1.0
Divertor ($230\ J \cdot cm^{-2}$)	Tungsten	5	A	NM	–
			U	NM	–
		20	A	NM	–
			U	NM	–
	Molybdenum	5	A	NM	–
			U	NM	–
		20	A	NM	–
			U	NM	–

[a] A = flux attenuation by vapour shield
U = No vapour shield attenuation
[b] NM = No melting occurs

for all materials, and the vaporization losses are generally reduced by factors of three to ten.

The effect of initial surface temperature on vaporization losses for graphite is shown in Tables VII-12 to VII-14. For the reference limiter conditions ($270\ J \cdot cm^{-2}$, 20 ms), the vaporization loss increases from $< 1\ \mu m$ to $9.2\ \mu m$ as the initial temperature is raised from 400 to 2400°C. Similar increases are predicted for the other disruption cases and materials which were considered [4]. Therefore, high operating temperatures are expected to result in higher material losses and shorter lifetimes.

TABLE VII-12. MAJOR DISRUPTIONS – CASE 2: HIGH LOAD TO LIMITER

	Material	Disruption Period (ms)	Disruption Model[a]	Melt layer thickness (microns)[b]	Vaporized depth (microns)
First wall ($35\ J \cdot cm^{-2}$)	Stainless steel	–	–	NM	–
	Beryllium	–	–	NM	–
	Tungsten	–	–	NM	–
	Graphite	5	A	–	<1.0
			U	–	<1.0
		20	A	–	<1.0
			U	–	<1.0
Limiter ($535\ J \cdot cm^{-2}$)	Beryllium (initial temp. 300°C)	5	A	120 ~ 150	6.6 ~ 14
			U	120 ~ 160	33 ~ 52
		20	A	155 ~ 160	0.5 ~ 2.1
			U	200 ~ 260	10 ~ 24
	Beryllium (initial temp. 900°C)	5	U	190	50
		20	U	320	32
	Tungsten	5	A	88	0.03
			U	120	0.22
		20	A	NM	–
			U	NM	–
	Molybdenum	5	A	110	0.06
			U	180	2.7
		20	A	NM	–
			U	NM	–
	Graphite (initial temp. 2400°C)	5	A	–	16
			U	–	37
		20	A	–	10
			U	–	31
	Graphite (initial temp. 400°C)	5	A	–	4.1 ~ 7
			U	–	21 ~ 28
		20	A	–	0.2 ~ 1.0
			U	–	3.2 ~ 13
	Pyrolitic graphite (initial temp. 300°C)	5	A	–	0.1
			U	–	0.26
		20	A	–	–
			U	–	–

Table VII-12 (cont.)

Material	Disruption Period (ms)	Disruption Model[a]	Melt layer thickness (microns)[b]	Vaporized depth (microns)
SiC	5	A	–	50
		U	–	110
	20	A	–	45
		U	–	110
New SiC	5	A	–	34
		U	–	92
	20	A	–	18
		U	–	72
Stainless steel	5	A	160	10
		U	150	42
	20	A	210	1.1
		U	260	17
TiC	5	A	–	–
		U	90	15.0
	20	A	–	–
		U	24	0.4
BeO	5	A	–	–
		U	32	32.6
	20	A	–	–
		U	65	11.2

[a] A = flux attenuation by vapour shield
U = no vapour shield attenuation
[b] NM = no melting occurs

8.3. Melt layer stability

Melt layer stability is a particular concern for stainless steel and beryllium because of the expected large melt layer thicknesses during disruptions. Any forces present during a disruption will act to move the melt layer, and if the forces are high enough, then part or all of the melt layer could be removed. The forces expected to dominate considerations of melt layer stability are magnetic forces that are produced when induced currents in the melt layer interact with the magnetic field. The magnetic forces depend both on the material properties and the geometry of the first wall and impurity control components. Geometric

TABLE VII-13. MAJOR DISRUPTIONS – CASE 3: REASONABLE LOAD TO LIMITER

	Material	Disruption Period (ms)	Disruption Model[a]	Melt layer thickness (microns)[b]	Vaporized depth (microns)
First wall ($170\ J \cdot cm^{-2}$)	Stainless steel	5	A	60 ~ 90	0.1 ~ 0.32
			U	90 ~ 110	0.38 ~ 2.8
		20	A	7 ~ 24	$<10^{-2}$
			U	7 ~ 24	$<10^{-2}$
	Beryllium (initial temp. 300°C)	5	A	60	0.2
			U	80	1.0
		20	A	NM	–
			U	NM	–
	Beryllium (initial temp. 900°C)	5	U	190	16
		20	U	240	5
	Tungsten	–	–	NM	–
	Graphite	5	A	–	<1.0
			U	–	<1.0
		20	A	–	<1.0
			U	–	<1.0
Limiter ($270\ J \cdot cm^{-2}$)	Beryllium (initial temp. 300°C)	5	A	84 ~ 100	0.33 ~ 1.1
			U	110 ~ 140	3.9 ~ 11
		20	A	40 ~ 70	–
			U	45 ~ 80	–
	Tungsten	5	A	NM	–
			U	NM	–
		20	A	NM	–
			U	NM	–
	Molybdenum	5	A	NM	–
			U	NM	–
		20	A	NM	–
			U	NM	–
	Graphite (initial temp. 2400°C)	5	A	–	5.4
			U	–	15.8
		20	A	–	1.6
			U	–	9.2

Table VII-13 (cont.)

Material	Disruption Period (ms)	Disruption Model[a]	Melt layer thickness (microns)[b]	Vaporized depth (microns)
Graphite (initial temp. 400°C)	5	A	–	0.8
		U	–	0.18
	20	A	–	<1.0
		U	–	<1.0
Pyrolitic graphite (initial temp. 300°C)	5	A	–	–
		U	–	–
	20	A	–	–
		U	–	–
SiC	5	A	–	–
		U	–	–
	20	A	–	–
		U	–	–
New SiC	5	A	–	8.9
		U	–	33
	20	A	–	0.59
		U	–	14
Stainless steel	5	A	120	0.6
		U	150	7.2
	20	A	130	<0.1
		U	130	<0.1
TiC	5	A	–	–
		U	19	<1
	20	A	–	–
		U	0	0
BeO	5	A	–	–
		U	35	5.1
	20	A	–	–
		U	3	0

[a] A = flux attenuation by vapour shield
U = no vapour shield attenuation
[b] NM = no melting occurs

TABLE VII-14. MINOR DISRUPTIONS

	Material	Disruption Period (ms)	Disruption Model[a]	Melt layer thickness (microns)[b]	Vaporized depth (microns)
Limiter (170 J·cm^{-2})	Beryllium (initial temp. 300°C)	5	A	50 ~ 60	0.04 ~ 0.21
			U	60 ~ 78	0.05 ~ 0.7
		20	A	NM	–
			U	NM	–
	Tungsten	–	–	NM	–
	Molybdenum	–	–	NM	–
	Graphite (initial temp. 2400°C)	5	A	–	1.9
			U	–	7.5
		20	A	–	0.45
			U	–	2.3
	Graphite (initial temp. 400°C)	–	–	–	–
	Pyrolitic graphite (initial temp. 300°C)	–	–	–	–
	SiC	5	A	–	11
			U	–	29
		20	A	–	6
			U	–	22
	New SiC	5	A	–	1.6
			U	–	13
		20	A	–	0.1
			U	–	0.5
	Stainless steel	5	A	90	0.14
			U	100	0.28
		20	A	9	–
			U	9	–
	TiC	5	A	–	–
			U	NM	0
		20	A	–	–
			U	NM	0
	BeO	5	A	–	–
			U	20	0
		20	A	–	–
			U	NM	0

[a] A = flux attenuation by vapour shield
U = no vapour shield attenuation
[b] NM = no melting occurs

TABLE VII-15. INSTABILITY INDEX FOR MELT LAYERS ON A Be LIMITER

Energy deposition ($J \cdot cm^{-2}$)	Disruption time (ms)	Instability index[a]			
		Limiter tip		Limiter centre	
		without	with cut	without	with cut
535	20	18.8	8.62	2.25	0.992
	5	15.5	6.87	1.18	0.436
270	20	0.0496	0.0118	3.5×10^{-5}	7.7×10^{-6}
	5	13.3	5.89	1.53	0.658
170	20	No melting		No melting	
	5	4.80	1.96	0.445	0.174

[a] Values much less than unity indicate stability. Values near unity indicate marginal cases.

considerations such as surface tile dimensions and current paths through the first wall will significantly affect the current in the melt layer and hence the melt layer forces.

The melt layer stability has been examined for the various impurity control designs. The stability analyses have utilized several modelling approaches. The first examines the force balance between the magnetic force perpendicular to the melt layer and the material 'internal forces' of surface tension and viscosity [2, 4]. This model is time-independent and considers the peak magnetic forces and peak melt layer thicknesses for the reference disruption times. A second model considers the Rayleigh-Taylor instability for droplet formation, and it includes the time dependence of the magnetic forces and melt layer thickness [1, 4]. The shift of the melt layer during a disruption has also been analysed with a time-dependent model [3]. Since the time-independent model considers only the peak forces and melt layer thicknesses, it is believed to be more conservative than the time-dependent model.

An example of the time-dependent analysis for a beryllium-coated limiter is shown in Table VII-15. For the reference disruption case (270 $J \cdot cm^{-2}$, 20 ms), the melt layer at the centre and tip of the limiter is predicted to be stable. At an energy density of 535 $J \cdot cm^{-2}$ or a disruption time of 5 ms, the melt layer at the centre of the limiter is predicted to be unstable or marginally stable. The major difference between the calculations for the limiter centre and the tip is assumed to be the lower energy density expected at the limiter tip which results in a thinner melt layer.

The results of these initial analyses indicate that melt layer stability is a concern for the surfaces exposed during a plasma disruption, and additional modelling and experimental effort is needed to fully understand this problem.

9. EROSION/RE-DEPOSITION

9.1. Introduction

Surface erosion is probably the most critical design issue for the impurity control system in INTOR, the other key issues being helium pumping and heat load. Erosion will result from sputtering, disruptions, and possibly arcing and other phenomena. Analysis of the surface erosion due to sputtering is complicated since, for INTOR conditions, many sputtered atoms return to the surface where they may stick as well as self-sputter. Therefore, the net erosion rate, i.e. sputtering minus re-deposition, determines the surface lifetime.

Erosion and redeposition of the surfaces of the pumped limiter and poloidal-divertor design was studied in detail. A broad range of materials options and plasma edge conditions were examined. The studies primarily made use of the US finite-difference impurity transport code, REDEP, [4, 15] and the USSR Monte Carlo impurity-tracing code [3]. The main conclusions of this study are the following:

(1) Most sputtered material is re-deposited, and so net erosion rates are usually much smaller than the gross rates.
(2) Low-Z materials (Be, C, BeO), for physical sputtering only, are acceptable at all plasma edge temperatures from the standpoint of plasma contamination.
(3) Medium- and high-Z materials (Fe, W) are restricted to low edge temperatures ($\lesssim$ 50 eV) because of self-sputtering constraints. At low temperatures, however, tungsten and tantalum are very attractive, yielding almost no net erosion.
(4) Erosion/re-deposition of the front face of the limiter and the entire divertor plate are similar.
(5) Erosion of the limiter leading edges is a problem at medium plasma edge temperatures, but several conceptual solutions exist. These are: (1) in-situ recoating of the leading edges and (b) use of a dual material limiter (e.g. W leading edge, Be front face).
(6) Research is needed in the areas of re-deposited material properties, edge temperature, and scrape-off conditions, and limiter leading-edge behaviour and optimization.

9.2. Computational models

Two computer models [3, 4, 15] were used to examine the net erosion of the limiter including the effects of the re-deposition on the limiter of the sputtered impurity ions. In these calculations, the plasma was fixed. The limiter erosion was calculated for sputtering by plasma ions, including deuterium, tritium, helium, and impurities. The transport of sputtered neutral impurity atoms was computed in the plasma. Once ionized in the plasma, the appropriate charge state of the impurity is

TABLE VII-16. PLASMA PARAMETERS FOR LIMITER EROSION CALCULATIONS

1. Plasma edge temperature (at start of scrape-off):
   Variable, $T_e = 20–1200$ eV
2. Transport power to limiter:
   $P_{TR} = 80$ MW, $T_e > 20$ eV
   6 MW, $T_e = 20$ eV
3. Charge-exchange power to limiter:
   $P_{cx} = 26$ MW
4. Plasma edge density (at start of scrape-off):
   $N_e = 2.5 \times 10^{19}$ m^{-3}, $T_e = 20$ eV

$$N_e = 0.5 \times 10^{19} \left(\frac{700 \text{ eV}}{T_e} \right)^{1.5} \text{m}^{-3}, \; T_e > 20 \text{ eV}$$

5. e-folding distances (at midplane):
   a) density, $\delta_N = 3.75$ cm
   b) temperature, $\delta_T = 3.75$ cm
   c) particle flux, $\delta_P = 2.5$ cm
   d) energy flux, $\delta_E = 1.5$ cm
6. Charged DT current to limiter:

$$L_{DT} = \frac{P_{TR}}{2 K T_e (1 + \gamma)} \frac{\delta_P}{\delta_E}$$

where the sheath factor $\gamma = 3.1$

determined, and the impurity ion travels back along the field line until it strikes the limiter again where it is deposited. The deposited ion also sputters more impurities (self-sputtering). The local net erosion is the local erosion of the surface due to sputtering minus the re-deposited impurity flux. The two codes include angular and energy-dependent sputtering coefficients and calculate the transport of the sputtered neutral impurity atoms in a two-dimensional geometry.

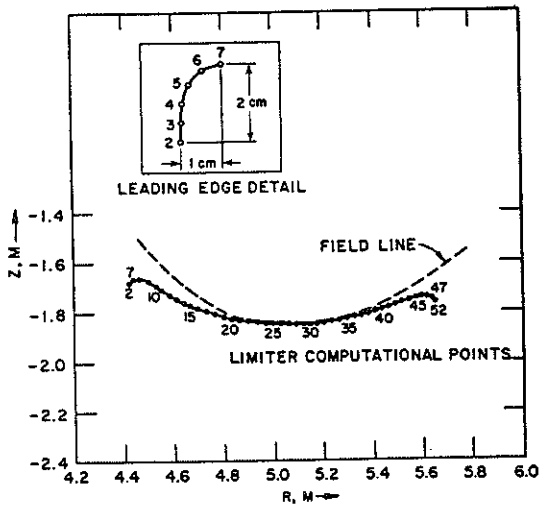

FIG. VII-39. Limiter model used for REDEP calculations.

9.3. Limiter analysis

The plasma parameters used for the limiter analysis are listed in Table VII-16. The constant-heat-flux, curved-bottom limiter shape shown in Fig. VII-39 was used for the calculations.

Edge temperature values of 700 and 100 eV were selected as reference values for 'high'- and 'medium'-edge-temperature operation, respectively. Figure VII-40 shows the behaviour of plasma temperature, total heat flux (transport plus charge exchange) and charged-(DT)-particle flux, Γ_{DT}, over the limiter surface, at $T_e = 700$ eV. (Note that, in these and other plots, limiter points may represent disproportionate areas with the leading edges represented by points 2–7 and 47–52, as shown in Fig. VII-40.) In general, the value of heat and particle flux depends on the respective e-folding distance and the limiter geometry. The heat flux is constant over the front face and falls off at the leading edges. Particle flux peaks at the leading edges which results in increased erosion there.

Figure VII-41 shows the various terms contributing to the net erosion of a Be coating at $T_e = 700$ eV. The total sputtering rate is the sum of the DT + α sputtering and the Be self-sputtering. As is shown, most of the re-deposition arises from the scrape-off zone, but a fair amount comes from material entering

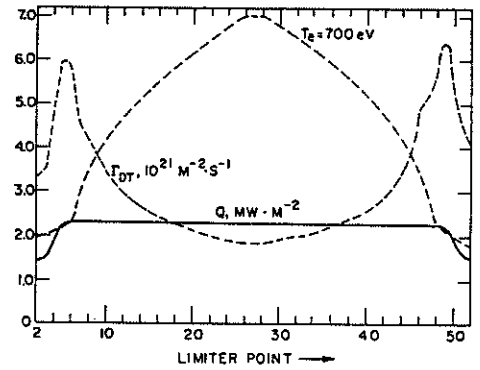

FIG. VII-40. Temperature, particle flux, and power flux across the limiter.

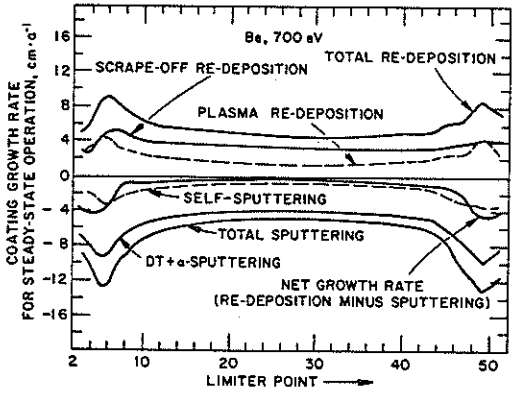

FIG. VII-41. Analysis of Be coating at 700 eV.

the plasma and then diffusing out. Re-deposition nearly balances sputtering over most of the limiter. The net erosion rate is fairly constant over the front face at <1 cm per year but increases to about 4 cm per year at the leading edges. All erosion/re-deposition rates in this subsection are given in units of centimetres per year of continuous operation (100% duty factor and 100% availability). For a 50% availability, erosion rates would be half these values.

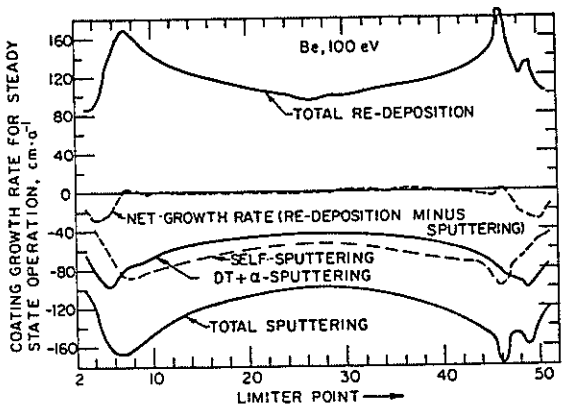

FIG. VII-42. Analysis of Be coating at 100 eV.

The situation at $T_e = 100$ eV is shown in Fig. VII-42. Both DT sputtering and self-sputtering are much greater than at 700 eV for two reasons: (1) the DT particle flux is seven times higher, and (2) sputtering coefficients are all closer to their peak values, particularly for self-sputtering. The fraction of sputtered material that is re-deposited, however (see Table VII-17), is higher at 100 eV than at 700 eV because the electron density is much higher. For example, at 100 eV, the mean free path of a Be atom, sputtered at the peak-in-the-distribution value of ≈ 1.5 eV, is only 0.6 mm at the limiter centre. Therefore, the net erosion rate over the limiter front face is only somewhat greater than at 700 eV.

At the leading edge, the re-deposition fraction is less than on the front face. This is, to some extent, due to longer mean free paths but is mostly a geometry effect, due to the small area of the leading edge and the angles of flux lines involved. At 100 eV, net erosion peaks at the leading edge at almost 30 cm per year.

Table VII-17 summarizes the REDEP results for runs for Be with $T_e = 20$ to 1200 eV. The last column in Table VII-17 is defined as the ratio of the current of Be atoms entering the plasma to the charged DT current to the limiter. The Be concentration in the plasma would be this value reduced (probably substantially) by the shielding efficiency of the plasma edge region. As shown, the average net erosion rate of the limiter decreases monotonically with increasing edge temperature but is reasonable even at low temperatures. Important considerations are, however, the uncertainties in the properties of the re-deposited material at high re-deposition rates as well as other model uncertainties. From the present REDEP calculations, however, the conclusion is that the front face of the limiter has acceptable net erosion rates for all plasma edge temperatures, but erosion at the leading edge is high.

TABLE VII-17. LIMITER – Be COATING – EDGE TEMPERATURE ANALYSIS

Edge temperature (eV)	Average sputtering rate ($cm \cdot a^{-1}$)	Average re-deposition rate ($cm \cdot a^{-1}$)	Average net erosion rate ($cm \cdot a^{-1}$)	Peak net erosion rate at leading edge ($cm \cdot a^{-1}$)	Average re-deposition fraction	Scrape-off shielding efficiency	Impurity contamination fraction (%)
20	23.5	22.0	1.5	6.9	0.94	0.77	2.0
100	122.1	120.8	1.3	29.4	0.99	0.98	0.3
300	25.1	23.9	1.2	16.7	0.96	0.85	1.5
500	10.6	9.7	0.9	8.4	0.91	0.71	2.2
700	6.2	5.5	0.8	4.7	0.88	0.58	2.7
1000	1.7	1.1	0.6	2.4	0.84	0.41	1.0
1200	2.8	2.4	0.5	1.6	0.82	0.36	3.2

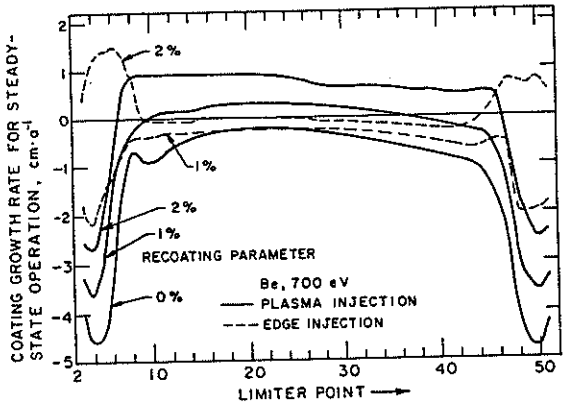

FIG. VII-43. Effect of in-situ recoating on the net growth rate of a Be-coated limiter.

Two conceptual solutions to the leading-edge problem were examined. The first is in-situ recoating. In this method, external Be atoms are supplied to the limiter by either of two means: (1) 'plasma injection' whereby beryllium is supplied to the plasma by gas puffing or pellets and (2) 'edge injection' whereby beryllium is injected into the scrape-off region near the leading edges. Both methods were simulated in REDEP for T_e = 700 eV, and the results are shown in Fig. VII-43. The injection parameter is defined as the ratio of external beryllium injected to the charged-DT current to the limiter. The curve with injection parameter equal to zero is the previous case at 700 eV. For plasma injections of 1 and 2%, net coating growth rates are achievable on the front face of the limiter. The leading-edge erosion is reduced, but there is still net erosion. For edge injection, however, the leading-edge erosion is changed substantially, and net growth can be achieved. By a combination of techniques and proper tailoring of the edge injection profile, it may be possible that the net growth/erosion rate could be held to very low values. Obviously, this would require experimental assessment.

A second proposed solution to the leading-edge problem involves the use of dual materials, a low-Z coating for the front face where self-sputtering must be limited, and a high-Z coating for the leading edge where low DT sputtering and high re-deposition is desired. A Be/W combination was assessed for T_e = 100 eV. Table VII-18 compares the dual-material scheme to the single-material case. Using tungsten at this leading edge, the rate of sputtering at the leading edge is reduced substantially, from about 138 to about 6 cm per year. (The rate is not zero because of charge-exchange sputtering.) Since tungsten is so heavy, the ionization mean free paths are very small, and the re-deposition rate is essentially 100%. Since the plasma

TABLE VII-18. SUMMARY OF DUAL-MATERIAL/SINGLE-MATERIAL LIMITER COATING – COMPARISON AT 100 eV EDGE TEMPERATURE

Parameter	Dual-material scheme	Single-material scheme
Coating material: front face	Be	Be
leading face	W	Be
Average sputtering rate – leading edge	6.4 cm · a^{-1}	137.5 cm · a^{-1}
Average re-deposition rate – leading edge	6.4 cm · a^{-1}	115.0 cm · a^{-1}
Average re-deposition fraction – leading edge	~ 100%	84%
Average net erosion rate – leading edge	~ 0 cm · a^{-1}	22.5 cm · a^{-1}
Peak net erosion rate – leading edge	~ 0 cm · a^{-1}	29.4 cm · a^{-1}

temperature at the leading edge is less than ≈ 50 eV, self-sputtering of tungsten is less than unity. This results in a zero net erosion rate. This scheme was only assessed at 100 eV but would clearly work at lower temperatures and at some higher temperatures. Other materials, particularly tantalum, might also be acceptable for the leading edge.

REDEP calculations were made for the limiter with carbon and beryllium oxide coating, and Table VII-19 compares these to the Be data for edge temperatures of 100 and 700 eV. Physical sputtering only was used for carbon (i.e. chemical sputtering was ignored). For BeO, equal amounts of Be and O sputtering were assumed, and equal sputtered-energy distributions based on a surface binding energy of 6.1 eV were employed. As is shown, the erosion results are quite similar for all three materials.

A key concern for BeO and other compounds is whether the surface coating remains as a compound or is gradually transformed to a single element. This should depend, in part, on the values of the re-deposited fluxes. Figure VII-44 shows the sputtered flux for oxygen and beryllium and the respective re-deposited fluxes at 700 eV. Although the re-deposited fluxes are nearly equal, they are not exactly so. The effect of this would have to be evaluated.

TABLE VII-19. LIMITER LOW-Z MATERIAL ANALYSIS

Coating material	Edge temperature (eV)	Average sputtering rate (cm · a^{-1})	Average re-deposition rate (cm · a^{-1})	Average net erosion rate (cm · a^{-1})	Peak net erosion rate at leading edge (cm · a^{-1})	Scrape-off shielding efficiency	Impurity contamination fraction (%)
Be	100	122.1	120.8	1.3	29.4	0.98	0.3
C[a]	100	104.5	103.1	1.2	22.6	0.96	0.5
BeO	100	129.2	127.0	2.2	22.1	0.96 Be 0.96 oxygen	0.4 0.4
Be	700	6.2	5.5	0.8	4.7	0.88	2.7
C	700	8.1	7.1	1.0	5.2	0.59	3.1
BeO	700	7.1	6.2	0.9	5.0	0.51 Be 0.59 oxygen	2.1 1.7

[a] Physical sputtering only.

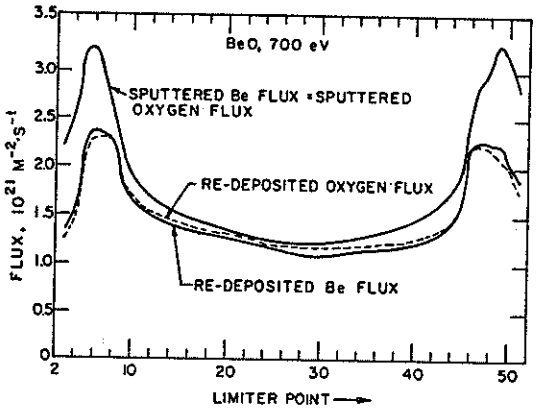

FIG. VII-44. Sputtered flux and re-deposited flux of Be and O to a BeO-coated limiter.

A tungsten coating was also evaluated. Tungsten suffers from a potentially severe self-sputtering problem whereby highly sheath-accelerated W ions can result in a runaway self-sputtering cascade. Estimates of the charge state of re-deposited tungsten ions were made (see Chapter VI) and the average predicted charge state is about four. Therefore, W ions acquire an energy of $\approx 12\ T_e$ in the sheath. The W ions also acquire some energy, through equilibration with the plasma, before the sheath is reached.

If a self-sputtering coefficient of unity is reached at an energy of 700 eV, typically indicated by experimental results, then this limits the acceptable edge temperature to less than 700/12 eV or about 50 eV. Even at this temperature, the self-sputtering is still substantial though finite. Figure VII-45 shows the result for a W limiter coating at 50 eV. Since the charged-DT sputtering coefficients are very small, practically all of the DT sputtering is from charge-exchange neutrals. Self-sputtering, in effect, amplifies the DT sputtering rate of about 10 cm per year to a peak value of about 60 cm per year at the limiter tip. The re-deposition rate is essentially unity, and so the net growth rate is predicted to be zero. There is also no leading-edge problem, and no tungsten reaches the plasma. Thus, although tungsten is restricted to a low-plasma-temperature regime, it yields very attractive results in this regime. This conclusion is the same for the divertor, with zero net erosion predicted for the outer collector plate at a separatrix plasma temperature of 50 eV.

The re-deposition calculations, using the Monte-Carlo code from Ref. [3], were made for a symmetrical concave limiter of r = 2.3 m and 1.5 m wide.

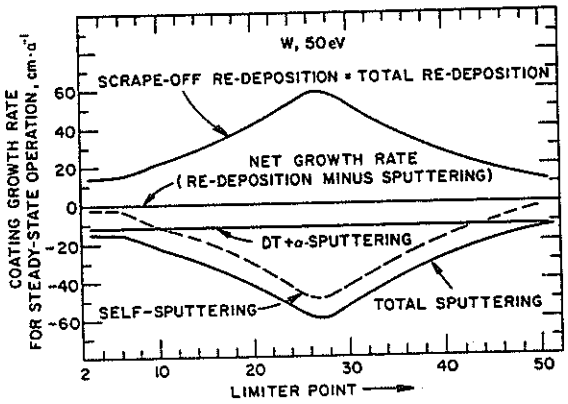

FIG. VII-45. Analysis of tungsten-coated limiter at 50 eV.

The calculations were made for three edge plasma modes: with low, high and medium temperature for the carbon-based alloy USB-15 and with medium temperature only for the Mo-alloy ZM-6 (Table VII-20). In the ZM-6 limiter, there is no erosion at low temperature as the energy of the ions incident on the limiter surface is less than the sputtering threshold. At high temperature, the self-sputtering coefficient for ZM-6 is more than one, and the code calculations give an infinitely rising flow of Mo atoms into the plasma. The calculation for medium temperature was made at a charge state of Mo equal to one. If the Mo-atom charge state is two, an infinite growth of the Mo-atom flow into the plasma takes palce. For a USB-15 limiter, the calculation results are obtained for all three modes and are presented in Fig. VII-46. The charge state of C atoms was assumed to be equal to 1 and 4, but the variation in the results for the two cases is negligible. The results of calculations show that re-deposition reduces the net erosion 1.5 – 10 times. A ZM-6 limiter is acceptable in the low-temperature regime only. A USB-15 limiter is acceptable at all three regimes, from the point of view of erosion.

9.4. Divertor

The plasma parameters used for REDEP analysis of the outer collector plate of the INTOR divertor plate were scaled, as necessary, from the data in Ref. [4], at 150 eV. The plate was modelled as a 1.0 m wide region extending from point 2 of the REDEP code as the left-hand boundary of the plate, point 27 as the centre (separatrix) and point 52 as the right-hand boundary. All points are linearly

TABLE VII-20. CHARACTERISTICS OF LIMITER MATERIAL RE-DEPOSITION

Reference parameters / Calculated parameters	Plasma mode	Low temperature		High temperature		Medium temperature[a]	
	Limiter flow	6×10^{23} s^{-1}		1.7×10^{23} s^{-1}		4.2×10^{23} s^{-1}	
	Ion energy	45		3000		600	
	Limiter material	USB-15	ZM-6	USB-15	ZM-6	USB-15	ZM-6
Maximum rate of gas ion erosion without re-deposition (mm · a^{-1})		8	0	25	indefiniteness	51	1.5
Maximum rate of erosion in self-sputtering and re-deposition (mm · a^{-1})		1.6	0	10		6	1.2
Maximum rate of thickness gain (mm · a^{-1})		1.3	0	8		6	0.7
Material atom flow to the first wall (s^{-1})		10^{19}	0	5×10^{19}		1×10^{18}	3×10^{16}
Material atom flow into plasma (s^{-1})		1.1×10^{21}	0	4.4×10^{21}		1.45×10^{21}	3×10^{19}
Mean concentration of limiter material particles in plasma[b] (%)		4.8	0	19.5		6.4	0.13

[a] Calculations here assume that the charge state of ions returned to the limiter is one. If the charge state is significantly greater than one, a runaway self-sputtering cascade is expected for ZM-6.

[b] Mean concentration of impurity particles in plasma is calculated on assumption of equality of particle flow into plasma from limiter and of flow of escaping particles from plasma due to diffusion.

FIG. VII-46. Analysis of USB-15 coating at various edge temperatures.

spaced. As is specified in Ref. [4], the flux on the plate is reduced by a factor of four due to the 15° inclination of the plate. Transfer of impurities from the divertor channel walls and the plasma to the plate, if any, was not modelled.

Figure VII-47 shows the divertor erosion for the case of a Be coating at a 100 eV separatrix temperature. Both DT sputtering and self-sputtering (not shown) tend to follow the non-symmetric Gaussian distribution of the charged-DT flux although the assumed spatially constant charge-exchange erosion somewhat spreads out the sputtering curve. The re-deposition rate (not shown) is almost identical with the sputtering rate over the entire divertor surface, and, therefore, the net growth/erosion rate is quite small. The effect of diffusion of returning impurities was also assessed. For a diffusion coefficient equal to the Bohm value, there is virtually no difference in the net growth rate. For a coefficient of 25 times Bohm, representing a substantial variation in the model, the net growth rate changes but is still less than ± 1.5 cm per year.

A similar analysis was carried out for a temperature of 700 eV. As with the limiter, the total sputtering rate is much less than at 100 eV, because of a seven-fold reduction in flux and a reduction in the sputtering coefficients. Since the plasma is more transparent to sputtered neutrals, the re-deposition fraction is less than at 100 eV and some beryllium is transported from the left-hand to the right-hand side of the plate and the right-hand channel wall. However, the net erosion rate is still quite modest. Thus, low-Z coatings appear to function well for the divertor plate over a broad range of edge temperatures.

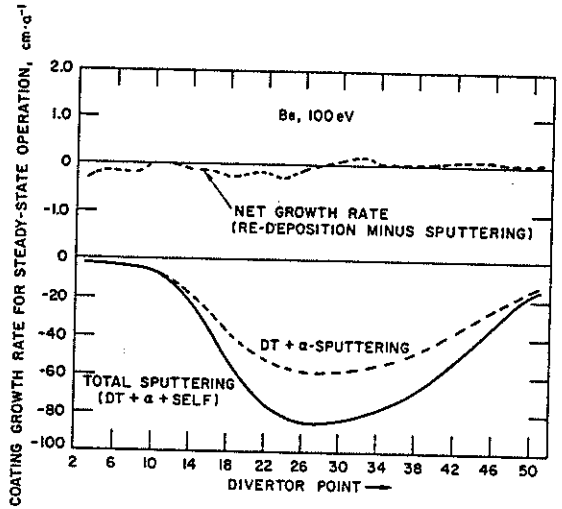

FIG. VII-47. Analysis of Be-coated divertor at 100 eV.

A tungsten coating was also examined for the divertor, at T_e = 50 eV. The result is the same as for the limiter, i.e. essentially complete re-deposition and no net erosion.

10. LIFETIME ANALYSIS

All parts facing the plasma are exposed to high heat flux. neutron irradiation, and erosion due to sputtering and disruptions. In the case of impurity control systems, the most important lifetime-limiting factor is erosion. The easiest way to cope with this condition would be to cover all parts with a sacrificial layer of sufficient thickness. However, an increase in thickness is accompanied by an increase in surface temperature and stresses, which can lead to melting, evaporation swelling and, eventually, to fatigue failure.

In the following, the limiter and the first wall near the limiter leading edges are treated separately. The maximum allowable temperature has been determined for the different materials. From this value and the known heat flux density, the maximum allowable thickness has been derived. Depending on the construction of the limiter, there may be parts, as for example the leading edge, where the maximum allowable thickness is limited by other properties. Taking the most

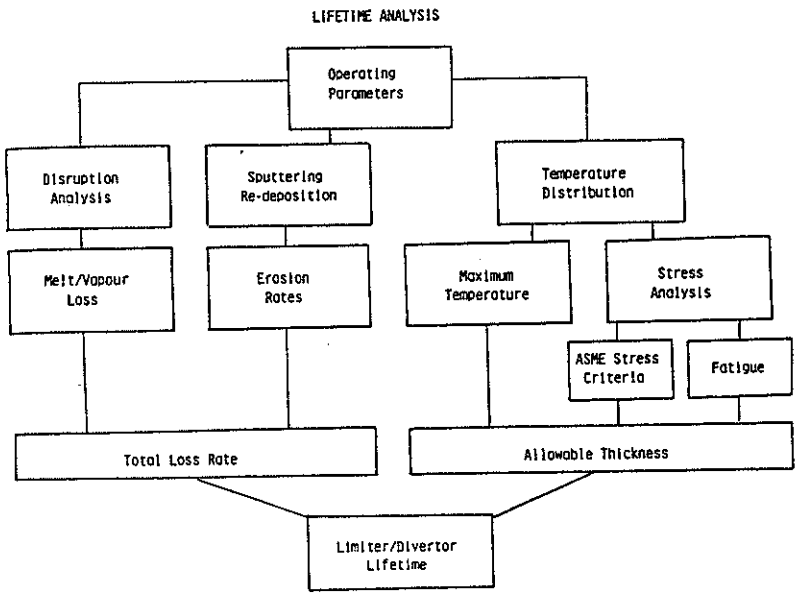

FIG. VII-48. Flow chart of lifetime analysis.

stringent conditions for the thickness and the net erosion rate, the lifetime of the limiter can be determined. Figure VII-48 represents schematically how to arrive at the lifetime.

10.1. Maximum allowable thickness

The maximum allowable thickness is determined by the maximum allowable temperature or the thermal fatigue limit whichever is more restrictive.

10.1.1. Maximum allowable temperature

The maximum allowable temperatures for the various materials are determined by:

(1) Melting
(2) Vaporization losses
(3) Excessive chemical sputtering

TABLE VII-21. MAXIMUM ALLOWABLE TEMPERATURES (K) OF SURFACE MATERIALS

Material	MP	Vaporization		Swelling	Chemical sputtering	Final
		1 mm · a^{-1}	10 mm · a^{-1}			
Be	1551	1130	1205	973	–	973
BeO	2823	1930	2055	> 873	–	> 873 <2000
C	3925	2170	2280	1173	773	773
SiC	2970	1620	1715	1473	–	1473
W	3683	2770	2950	< 873 >1173	–	873
Ta	3269	2600	2770	< 773 >1073	–	773
SS	1773			> 643	–	643

(4) Radiation-induced swelling/cracking
(5) Microstructural changes (e.g. sintering, phase changes).

For the present analysis, all the criteria except for microstructural changes have been considered. The results of the analysis are presented in Table VII-21.

In most cases, the allowable temperatures are limited by radiation damage considerations. For beryllium, high helium bubble swelling is observed at temperatures higher than 973 K, and for SiC significant swelling rates are observed at temperatures $\geqq$1473 K [16, 17]. In the case of tungsten and tantalum, radiation swelling peaks are observed at relatively low temperatures [18, 19]. BeO is a special case, because it is an insulator with a non-cubic crystal structure. At low temperatures, radiation swelling is rapid and anisotropic, which results in micro-cracking of polycrstalline material [20]. Models and limited data suggest that the degree of swelling decreases at elevated temperatures, and it should remain at acceptable levels above about 873 K. Therefore, BeO also has a minimum operating temperature in addition to a maximum one. It should be noted that for radiation-limited temperatures, there are often only limited data from which to determine temperature limits. The temperatures shown in Table VII-20 may be modified in the future as additional data become available.

However, the maximum temperatures are reached on the surface only. Since the thickness is constantly reduced and the swelling appears only after considerable

TABLE VII-22. ALLOWABLE THICKNESSES (TEMP.) SURFACE MATERIALS

Material	Allowable thickness	
	Unirradiated (cm)	Irradiated (cm)
Be	2.5	2.5
BeO	4.5	2.4
C	1.5	0.4
SiC	1.4 >5 (Hi K)	1.0
W	3.6	3.6
Ta	3.2	3.2

neutron irradiation, the limitation of the thickness by the criterion applied here is very conservative and needs further elaboration.

The only material whose operating temperature is limited by chemical sputtering is graphite. The chemical-sputtering peak for hydrogen-bombarded graphite is ≈873 K, and recently temperature-dependent sputtering has been observed at temperatures above ≈1273 K. To remain below the peak sputtering temperature, the graphite temperature limit has been set at ≈773 K. Other materials, particularly the carbides, may also exhibit chemical sputtering, but the effect is expected to be minor compared to graphite. Chemical sputtering was discussed in greater detail in Section 4.

10.1.2. Allowable thickness

The information presented in the previous section, along with the heat flux density and the thermal conductivity, can be combined to determine the thickness limited by the temperature criterion. Table VII-22 shows the temperature limited thickness for the top surface materials in both unirradiated and irradiated conditions. The heat flow assumed at the limiter surface was 2.4 MW · m^{-2}, the coolant temperature was 100°C and perfect conduction at the interface between tile and heat sink was assumed. The difference for the materials in the irradiated and unirradiated conditions is the reduced thermal conductivity in non-metals which is observed following irradiation. It has been assumed, for the purpose of comparison, that the effect of radiation is to reduce the thermal conductivity to 30 W · mK^{-1} as has been observed for graphite [1]. This assumption was made

TABLE VII-23. ALLOWABLE THICKNESS OF LEADING EDGE

Material	Temperature-limited		Fatigue-limited	
	Cu (cm)	V (cm)	Cu (cm)	V (cm)
Be	3.2	2.6	0.5	2.1
BeO	>4	3.2	0.6	2.2
C (unirr.)	2.4	1.7	–	–
SiC	2.1	1.7	0.35	1.7
W	2.8	2.2	0.2	0.9

because of the very limited data available for other non-metals. The actual thermal conductivity following irradiation could be greater or smaller than this value. The reduction in conductivity with irradiation is rapid, with saturation levels reached after a damage level of only about 1 dpa.

Changes in the mounting techniques will strongly affect the heat conductivity across the boundary between heat sink and protective layer and therefore the allowable thickness.

The leading-edge allowable thicknesses are different from the top surface thicknesses, because of different geometries. The cylindrical geometry results in a different temperature distribution and in more severe stress constraints than the plate geometry. The results for equivalent calculations of allowable thicknesses are shown in Table VII-23. These values are calculated for an outer radius of 1.5 cm of the leading edge and a heat flux density of 1 MW· m^{-2}. The table makes a distinction between a copper and a vanadium heat sink. No values are given for irradiated materials. Preliminary calculations on the limitations of the allowable thickness by thermal fatigue have shown that the constraints are much more severe at the leading edge. In this case a major difference may arise between copper and vanadium as heat sinks as can be seen from columns 3 and 4 of Table VII-23.

10.1.3. Other limiting factors

The surface temperature is one of the most important features limiting the thickness of the protective layer. Fatigue of the whole structure is in some parts even more limiting as has been shown in Table VII-22. However, its influence is strongly dependent on the specific design and has to be considered separately

TABLE VII-24. PREDICTED SPUTTERING/RE-DEPOSITION RATES FOR THE LIMITER TOP SURFACE (cm · a^{-1} AT 50% AVAILABILITY)

Material	Edge temperature						
	20	100	300	500	700	1000	1200
Be	0.75	0.65	0.60	0.45	0.40	0.3	0.25
BeO	–	1.10	–	–	0.45	–	–
C	–	0.60	–	–	0.50	–	–
SiC	0.40	–	n.a.	n.a.	n.a.	n.a.	n.a.
W	0	–	n.a.	n.a.	n.a.	n.a.	n.a.
Ta	0	–	n.a.	n.a.	n.a.	n.a.	n.a.

for every design. Optimization will be possible. Changes in properties due to neutron irradiations have been considered only as far as thermal conductivity of the protective tile is concerned. Mechanical and fatigue properties of the structure will be changed, as well. The different factors affecting the lifetime are not necessarily independent. For example, any decrease in the thickness of the protective layer due to sputtering reduces the thermal stresses on the heat sink and increases its fatigue life.

Fatigue failures in the surface material do not hamper the availability of the limiter, but may influence the lifetime of the heat sink. The lifetime of the attachment is another feature which should be included in the consideration.

10.2. Lifetime estimates

Different estimates are necessary for the limiter plate top surface, the leading edges, the first wall and the strips of the first wall close to the limiter edges. In the following, the lifetimes are derived from the maximum allowable thickness and total erosion rates.

10.2.1. The limiter top surface

As was shown in Section 9, the net erosion at the limiter top due to sputtering is rather low as long as re-deposition is considered. The erosion rates for different materials are given in Table VII-24 [4].

TABLE VII-25. LIFETIME OF LIMITER TOP SURFACE

Material	Allowable thickness	Edge temperature	Total erosion rate			Lifetime		
			Stage I	Stage II	Stage III	Stage I	Stage II	Stage III
	(cm)	(eV)	($cm \cdot a^{-1}$)			(a)		
Be	2.5	20	0.85	0.5	1.0	3	5	2.5
		100	0.8	0.45	0.9	3	5	2.6
		700	0.72	0.32	0.64	3.4	8	4
BeO irradiated	2.4	20	–	–	–			
		100	0.35	0.55	1.1	8	4.2	2.2
		700	0.15	0.25	0.45	16	10	5
C irradiated	0.4	20						
		100	0.20	0.30	0.6	2	1.3	0.7
		700	0.17	0.25	0.5	2.2	1.6	0.8
SiC irradiated	1.0	20	0.37	0.18	0.23	3	5.5	4.3
W	36	20	–	–	–	8	8	8
Ta	3.2	20	–	–	–	8	8	8

TABLE VII-26. LIFETIME (YEARS) – STAGE III LEADING EDGE (V-15Cr-5Ti HEAT SINK)

Material	Sputtering		Sputtering and disruptions			
			Reference		Worst case	
	100 eV	700 eV	100 eV	700 eV	100 eV	700 eV
Be	0.1	0.9	0.1	0.9	0.1	0.7
BeO	0.1	0.9	0.1	0.9	0.1	0.8
C	0.1	0.8	0.1	0.8	0.1	0.8
SiC	0.2[a]	–	0.2[a]	–	0.2[a]	–
W	∞[a]	n.a.	∞[a]	n.a.	∞[a]	n.a.
Ta	∞[a]	n.a.	∞[a]	n.a.	∞[a]	n.a.

[a] 50 eV.

The erosion due to disruptions depends on energy density, the disruption time and the number of disruptions. In Table VII-14, these values are given. Only for beryllium have we to expect an important contribution from disruption. The combination of both tables yields the lifetimes shown in Table VII-25.

10.2.2. The leading edge

At the leading edge, the disruptions are assumed to be negligible; therefore, the lifetime is entirely determined by the sputtering. Since the surface thickness has to be kept low, because of fatigue problems, the lifetime appears to be rather short, as is shown in Table VII-26.

10.2.3. The first wall

During Phase One, the lifetime of the first wall had been considered for a case corresponding to the medium-temperature case of our operational conditions (Section 2). It had then been concluded that the maximum thickness is limited to 13 mm by fatigue at a heat flux of 40 MW. For the disruption, it had been assumed that the melt layer was stable. The discussions which took place during Phase Two A showed the fundamental uncertainty of how to consider the influence of disruptions and, more specifically, the behaviour of the melt layer. Further large variations are generated by the uncertainties in the disruption time. Finally, the

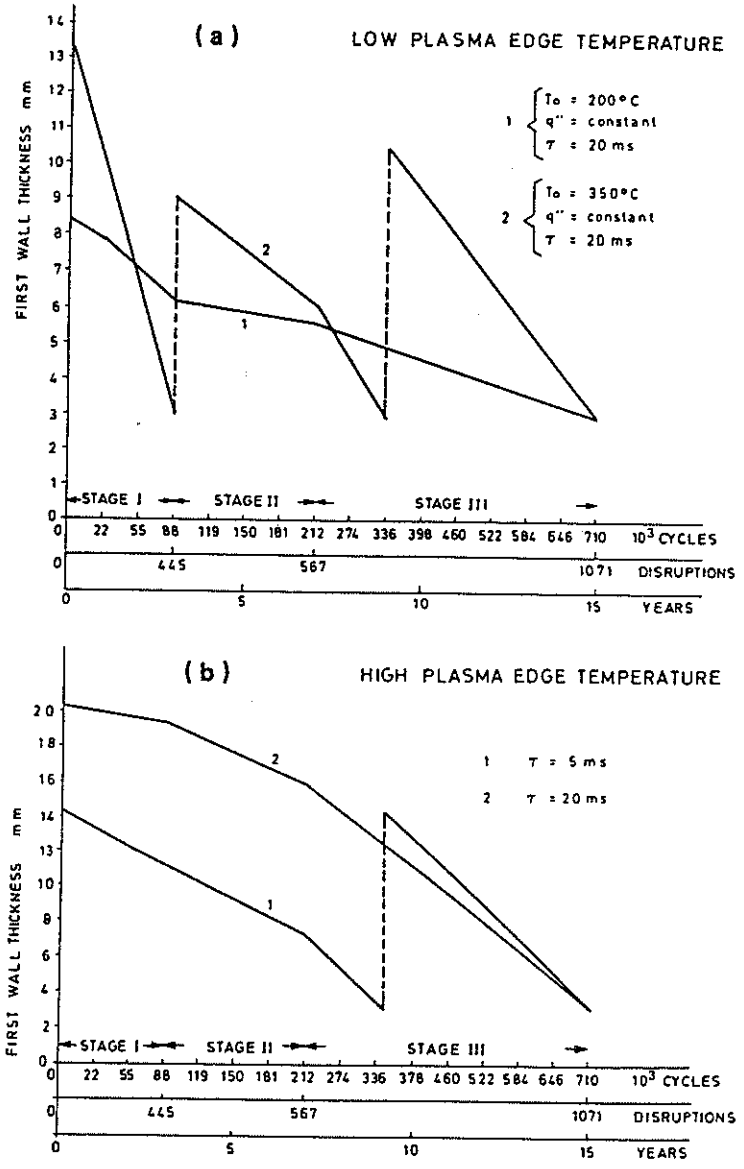

FIG. VII-49. Replacement sequence of the first wall.

TABLE VII-27. SPUTTERING FROM THE FIRST-WALL STRIPS NEAR THE LIMITER TIPS

	Low edge temperature	Medium edge temperature	High edge temperature
Neutral flux density ($m^{-2} \cdot s^{-1}$)	5.2×10^{21}	2.7×10^{21}	2.8×10^{20}
Particle energy (eV)	20	300	2900
Sputtering coefficients:			
D	0	1.7×10^{-2}	2.2×10^{-2}
T	0	3.2×10^{-2}	4.5×10^{-2}
He	0	8.4×10^{-2}	12.6×10^{-2}
Total	0	2.7×10^{-2}	3.8×10^{-2}
Erosion rate ($m \cdot s^{-1}$)	0	8.8×10^{-10}	1.3×10^{-10}

results are strongly affected by the temperature of the first wall at the beginning of the disruption (the differences for stainless steel in Table VII-14 are due to this fact). A number of approximations have shown that melt layers of 24 μm on stainless steel, which form only during the last phase of the disruption, are stable. In this case, no erosion occurs at the first wall, and its lifetime is more than 15 years. Using the assumption of a totally lost melt layer, the new disruption scenarios, and the higher value for stainless steel in Table VII-14, it turns out that the thickness of the first wall lost by disruptions during the reactor life is about 15 mm. Therefore, it would be necessary to exchange the first wall at least once (sacrificial layer foreseen: ≤10 mm). In the case of high edge temperature, the heat load on the first wall is about half of the reference case. Therefore, the problem of fatigue is partly mitigated but the disruption erosion is still about 15 mm and would need one replacement. At low edge temperature, the heat load is considerably increased. Consequently, the temperature will be higher and lead to higher erosion and fatigue damage. The situation of replacements is given in Fig. VII-49. About three replacements appear to be necessary.

10.2.4. First-wall strips

In contrast to the divertor configuration, sputtering by neutrals on the first wall, in the case of a limiter, is concentrated on the strips near the leading limiter edges. Table VII-27 gives the sputtering rates in the strip regime for the three cases.

The erosion of the strip region due to disruption has been neglected since it is assumed that the limiter will protect these zones. From Table VII-27 it follows:

- For the low-temperature case, no sputtering is expected, and, therefore, the strips can be made sufficiently thin in order to cope with the high heat flux.
- In the case of medium edge temperatures, sputtering is very high. For about 10 mm thick sacrificial layers, replacement will be necessary every year.
- At high temperatures, the lower sputtering and the lower heat flux are much less severe conditions, and, therefore, only a single replacement is needed during the lifetime of the machine.

10.3. Conclusions

The lifetime has been analysed for the limiter top surface, the leading edge, the first wall and the first-wall strips along the limiter edges.

Three distinct cases have been looked at:

(i) In the low-edge-temperature case, it is possible to build a limiter protected with high-Z materials which can last the whole lifetime of the reactor. The first wall has to be replaced twice, owing to the erosion by disruptions. The strip at the limiter edges will last sufficiently long if the assumption that disruptions do not touch this area is correct.

(ii) At medium edge temperatures, solutions can be found for the limiter top surface which needs an exchange every two to five years. The leading edge will have an acceptable lifetime only if it can be made of high-Z materials. The first wall will probably have a lifetime of more than 15 years. However, the strip of the first wall along the limiter edges will be rather short-lived (about one year).

(iii) The high-edge-temperature case can be solved at the limiter surface by using low-Z materials achieving lifetimes of the order of three to five years. In this case, the leading edge will have an extremely short lifetime (about 8–10 months). First wall and first-wall strip are not critical. One exchange will be sufficient to make them last for the entire reactor lifetime.

11. RECOMMENDATIONS ON DESIGN CONCEPTS

11.1. Introduction

Impurity control in INTOR is provided by either a single-null poloidal divertor or a double-edged, pumped limiter that is shaped to evenly distribute

the heat flux. Either component would be located at the bottom of the plasma chamber. The focus of the effort during Phase Two A has been on the designs of the limiter blade and the divertor collector plate which are the structures that experience the most severe conditions. Design solutions for these components have been identified for different plasma edge conditions.

The primary considerations for design are the plasma-surface interactions and the component strength requirements. For the cases examined, the materials with desirable surface properties are not generally considered to be appropriate structural materials. Therefore, all designs have utilized duplex structures consisting of an actively cooled heat sink upon which a plasma-side material is bonded. The attachment of the plasma-side material to the heat sink is a critical issue that greatly impacts the performance and reliability of the engineering design. A high-thermal-conductance bond, recommended as the reference attachment scheme, can produce large stresses across the interface because of the mismatch in the physical properties of the plasma-side and heat sink materials. The selection of the plasma-side material is based upon the plasma environment at the plate, and the selection of the heat sink material is based primarily on strength, thermal conductivity, and fabrication requirements.

11.2. Divertor

The overall configuration of the poloidal-divertor concept is shown in Fig. VII-1. The divertor is located at the bottom of the plasma chamber with a continuous toroidal opening extending around the reactor. The divertor is divided into removable modules. There are 24 modules, two for each TF coil. These modules are removable so that the divertor collector plates can be replaced without removing an entire torus sector. This is required because it is anticipated that replacement of the divertor collector plates will be more frequent than that of the first wall. Access limitations of 12 TF coils require use of two modules per sector to allow removal. The divertor module does not incorporate breeding at this time, but it can be included if required.

The divertor collector plates are set at an angle with respect to the magnetic field lines in order to limit the peak heat flux to about 2 $MW \cdot m^{-2}$. For the inner channel, which has a peak heat flux of 4 $MW \cdot m^{-2}$ normal to the separatrix, the plate is placed at an angle of 30° to the field lines. For the outer channel, which has a peak heat flux of 8 $MW \cdot m^{-2}$ normal to the separatrix, the plate is placed at an angle of 15° to the field lines. Shaping of the collector plates could produce a constant heat flux over a portion of the surface, but a compound curvature would be required. Since the peak heat flux is already quite manageable, shaping does not appear to be necessary.

11.2.1. Low-edge-temperature regime

There is a significant probability that the plasma will be cooled along the divertor channel to the point where T_e at the plate is only about 30 eV (see Chapter VI). Under these conditions, high-Z materials appear to be particularly attractive as plasma-side material. Sputtering/re-deposition calculations indicate that in this regime the net erosion of high-Z materials is almost zero. Practically all of the remaining sputtering which occurs is caused by charge-exchange neutral and self-sputtering by returning high-Z particles. The sputtered particles are predicted to be re-deposited, however, such that the net erosion rate is close to zero. A critical parameter in this analysis is the self-sputtering coefficient. Re-deposition models predict a runaway self-sputtering cascade when the self-sputtering coefficient exceeds unity. For high-Z materials, this point is reached at energies in excess of 500–1000 eV. When the accelerating effect of the sheath potential ($\approx 3\ T_s$) and the charge state of the ionized particles (≈ 4) are taken into account, the plasma temperature at the plate is limited to < 50 eV to ensure that self-sputtering is less than unity.

Tungsten has been selected as the reference high-Z material for use in the low-temperature regime. It exhibits the highest energy at which self-sputtering exceeds unity, and because of its high melting point, it is particularly resistant to the disruptions postulated for INTOR. Tantalum and molybdenum are expected to behave in a fashion similar to tungsten and are considered to be alternate materials in this application.

It should be noted that it may be possible to utilize tungsten in the divertor even when the self-sputtering coefficient exceeds unity. There are two reasons why this may be possible. First, if a large amount of sputtered tungsten particles enters the plasma above the plate surface, they will cool the plasma by increasing the amount of energy radiated to the walls of the divertor chamber. As the plasma cools, the amount of self-sputtering will be reduced until an equilibrium is established. At this point, the amount of tungsten lost from the surface would presumably be equal to the amount of tungsten needed to maintain the impurity cloud above the surface of the plate. Second, if a significant portion of the sputtered tungsten atoms is not ionized by the plasma, but is lost by depositing on the walls of the divertor chamber, then it is possible to operate with self-sputtering greater than unity and still not predict a runaway self-sputtering cascade. The major concern with these concepts is the possibility that a large amount of tungsten impurities could escape into the plasma chamber. Neither concept has been established, so that they must be considered to be speculative for the time being. Further work should, however, be performed in this area.

The heat sink material is required to have adequate strength, good thermo-physical properties to accommodate the high heat fluxes, reasonable fabricability, and resistance to radiation up to damage levels of 20 dpa. The materials for

which the largest amount of experience is available for high heat flux applications are copper and copper alloys so that they are selected as reference heat sink materials. Several possible alloys exhibiting acceptable physical and mechanical properties are commercially available. Little is known, however, on the effects of radiation to high fluence levels, particularly in the area of radiation embrittlement, and it is not possible to select a single reference alloy until more information is obtained. Also, because of the complicated nature of duplex plate designs, a considerable amount of development is needed to demonstrate the fabrication of prototype structures using copper alloys. Vanadium and zirconium alloys are considered to be alternate heat sink materials. The V-15Cr-5Ti alloy has fatigue properties superior to those of copper alloys, but it is not commercially available, and considerable development is required to establish the engineering data base. Zirconium alloys are commercially available, but they may be susceptible to hydrogen embrittlement in the INTOR environment.

11.2.2. Medium-edge-temperature regime

Another likely condition at the divertor plate is a plasma temperature of about 100 eV. At this energy, the self-sputtering coefficients of high- and medium-Z materials will exceed unity at the collector plate, and they are thus not considered to be usable in this regime. Only low-Z materials, for which the self-sputtering coefficients never exceed unity, are considered acceptable.

Estimates of the sputtering and re-deposition for low-Z materials indicate that a loss of material from the surface at the rate of $\frac{1}{2}$ cm per year is possible in this regime. To maximize the collector plate lifetime, it is desirable to make the plasma-side material as thick as possible. The thickness is restricted by temperature limitations of the material and by stress limitations through the plate structure. Of the different materials considered, beryllium is calculated to have the longest lifetime for INTOR operating conditions; it is selected as the reference material in this regime. The alternate surface material is graphite, which is predicted to have a considerably shorter lifetime. The shorter lifetime is due to the severe temperature (and thickness) limitations that are required to avoid chemical sputtering. Graphite has other desirable properties including resistance to plasma disruptions and low induced thermal stresses under high-heat-flux conditions. If chemical sputtering could be eliminated, graphite would become a more desirable material to use. Radiation damage would then probably limit its useful life.

The heat sink material would again be a copper alloy. With beryllium as the plasma-side material, a high-strength alloy, such as a Cu-Be alloy, would be required to accommodate the stresses due to the property mismatch with beryllium. If graphite were used, any copper alloy, including annealed pure copper, is capable of accommodating the stresses. Additional strength, if needed, could be added by backing the copper with a high-strength stainless steel.

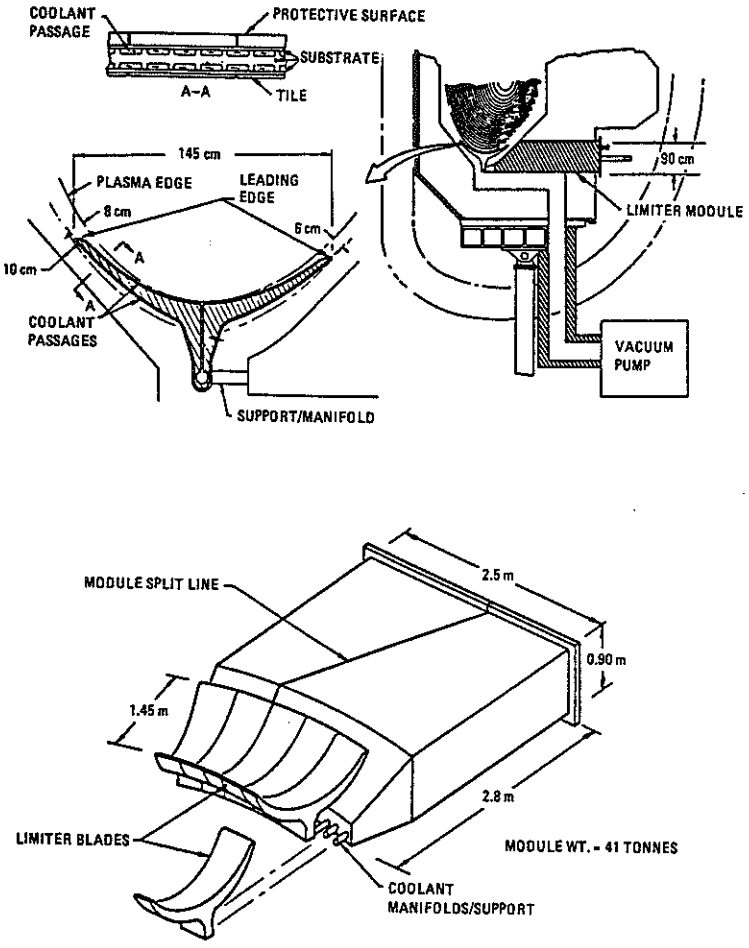

FIG. VII-50. Shaped, double-edged-bottom limiter.

11.3. Limiter

The reference limiter design is a curved, double-edged pumped limiter located at the bottom of the plasma chamber. An example of this design is shown in Fig. VII-50. The concept utilizes a removable limiter module. One module is used in each of the 12 reactor sectors. As with the divertor module, the module is split into two segments so as to allow removal. Each module consists of six replaceable limiter blade segments, mounted by coolant manifolding to the main body of the module.

The limiter blade has a concave shape facing the plasma. The front surface contour is based on physics calculations to obtain a uniform heat flux of ≈ 2 MW$\cdot$m^{-2} over the surface. This results in a surface that is not symmetrical because of the spreading of flux lines at the bottom of the plasma. The overall width of the blade is ≈ 145 cm. The back surface of the limiter is contoured such that flux lines do not impinge on the blade until they contact the neutralizer plate near the centre. The pumping channel behind the blade is set at 10 cm and extends for approximately 60 cm behind each edge. The blade thickness varies from approximately 3 cm at the leading edges to 10 cm near the neutralizer plate. The thickness can be increased or decreased so as to accommodate the electromagnetic loads; the thickness of the leading edge should, however, be as small as possible to maximize the pumping capacity. The thickness of the centre section (neutralizer area) can also be altered to a certain extent, but adequate room must be allowed for supply and return water manifolds. The vertical position of the mounting support/manifolding is located beyond the outermost flux line in order to prevent excessive heating by incoming particles.

The blade consists of a water-cooled substrate covered by protective tiles. Water channels run in a poloidal direction over the entire limiter including the back and neutralizer area. Manifolding is located in the bottom centre section and connects to the main supply manifold/support struts. Coolant channels follow the back of the limiter to the leading edges, to the front centre and then through passages leading to the return manifold.

11.3.1. Low-edge-temperature regime

Low plasma edge temperatures with $T_s \approx 10$ eV have been examined for limiter designs. Since this environment is similar to the low-temperature divertor regime, the design solution for the limiter blade is similar to the divertor collector plate. Tungsten bonded to a copper alloy plate is the reference material for the low-edge-temperature conditions. The net erosion caused by sputtering and disruptions is calculated to be negligible for the INTOR conditions. An alternate design is also possible in this regime. The amount of power to the limiter is only ≈ 22 MW (compared with 84 MW at the medium edge temperature), and

austenitic stainless steel may be considered to serve as structural material in spite of its poor thermophysical properties. The alternate low-edge-temperature design consists of an array of bare stainless-steel tubes (see Fig. VII-24). The use of bare tubes eliminates the problems of duplex structures, but the tubes are susceptible to disruption damage that could result in very short lifetimes.

11.3.2. Medium-edge-temperature regime

The medium-edge-temperature regime with $T_s \approx 150$ eV is similar to the medium-temperature case for the divertor. Low-Z materials must again be used on the surface. For the reference INTOR conditions, beryllium is predicted to have the longest lifetime and is selected as the reference plasma-side material. Graphite is the alternative surface material, and a copper alloy is recommended for the heat sink material.

The limiter, in this regime, has a problem that does not occur in the divertor. The leading edge of the limiter is predicted to undergo rapid erosion ($\approx$ 29 cm per year), because of physical sputtering. Design modifications have been considered to alleviate this problem. The first modification involves the replacement of the beryllium on the leading edge with a high-Z material such as tungsten. The plasma temperatures at the leading edge are lower than 50 eV, where the net erosion of tungsten is predicted to be negligible. The second modification involves the injection of Be particles into the edge of the plasma. Model calculations indicate that a sufficient quantity of beryllium can be injected to produce a net build-up of material on the leading edge and still not significantly affect plasma operation. Both modifications require additional development effort.

12. CONCLUSIONS AND RECOMMENDATIONS

The major conclusions and recommendations are summarized as follows:

(1) Impurity control remains a major issue in the design of tokamak reactors. The two leading candidates, a poloidal divertor and a pumped limiter, each have considerable uncertainties. The divertor appears to have advantages in impurity control and helium pumping. However, the magnetic system necessary for the divertor introduces considerable complexity to the reactor relative to that with a limiter. Uncertainties in the scrape-off conditions, erosion by physical sputtering, disruptions and arcing, and in re-deposition of eroded materials make prediction of the lifetime of the limiter and divertor plate very difficult.

(2) A poloidal divertor design has been developed for INTOR. Analysis shows that it should provide adequate control of impurities and acceptable helium removal capability. The overall magnetics design is acceptable but additional analysis is required to establish the specific characteristics of the separatrix control coils. Angling of the divertor plates relative to the field lines is necessary to reduce the peak heat flux to about 2–3 MW$\cdot$m^{-2}.

(3) A pumped limiter design has been developed for INTOR. Two-channel pumping and shaping of the limiter are necessary to achieve adequate pumping while maintaining the peak heat flux of about 2–3 MW$\cdot$m^{-2} on the surface and of about 1–2 MW$\cdot$m^{-2} at the leading edges. Peak heat fluxes are sensitive to plasma edge conditions and plasma position.

(4) The three plasma edge regimes which have been evaluated can be characterized by a plasma edge temperature over most of the scrape-off region and a sheath plus pre-sheath temperature T_s in the immediate vicinity of the surface of the divertor target or limiter plate. The results of the evaluation can be summarized as follows:

A. Edge temperatures above 700 eV reduce erosion of low-Z materials. Temperatures above 700 eV might be realized by reducing the edge density with pellet injection and high pumping efficiency. In this regime, T_s tends to be equal to the edge temperature. However, the INTOR participants judge that the realization of the high-edge-temperature condition is rather uncertain so that it would be imprudent to base the design on this condition.

B. The medium-edge-temperature regimes ($\approx$ 100 eV away from the plate) is the most likely condition if radiation from impurities does not reduce the temperature. In conditions where the scrape-off layer is thin, T_s tends to be equal to the edge temperature and the erosion is very severe. This condition is more likely in the case of a limiter ($T_s \approx 100$ eV). In conditions where the scrape-off thickness is comparable to the values quoted in Table VII-4, T_s is likely to be lower than the edge temperature (typically, 30 eV) and this condition is more likely for the divertor. Achieving a reasonable lifetime for the limiter and divertor plate requires experimental verification of the prediction that most of the eroded materials will be re-deposited and that the properties of the re-deposited material are acceptable.

C. Low edge temperatures ($<$ 50 eV) might be obtained with high edge radiation, and in this condition T_s could be as low as 10 eV. However, the physics feasibility of attaining the low-edge-temperature conditions remains to be established experimentally. Limiter and divertor plate lifetimes can be relatively long if disruption-resistant high-Z materials are used.

(5) The selection of reference materials for the high-heat-flux components depends on a number of criteria aiming at maximizing the component lifetime. In particular, the selection of the plasma-side materials depends strongly on the plasma conditions in the vicinity of the plate and the charge state of

impurity ions striking the plate. The charge state is estimated to be about two to three for low-Z materials and about three to four for high-Z materials. The plasma-side materials considered are W, Ta, Mo, Be, BeO, C, SiC, and TiC. For a pre-sheath plasma temperature, $T_s < 50$ eV (ion energies $< 400-700$ eV), high-Z materials such as tungsten, tantalum, or molybdenum are viable and preferable because of low erosion and good resistance to disruptions. Tungsten is the preferred high-Z material. At ion energies larger than 400–700 eV, the self-sputtering coefficient of all medium- and high-Z materials exceeds unity, and therefore a runaway sputtering cascade is predicted. Thus, for energies larger than 50 eV only low-Z materials (C, B, Be, B_4C, BeO, and possibly SiC) are viable since their sputtering yield never exceeds unity. Beryllium is the preferred low-Z material based on lifetime considerations. All materials have some undesirable properties. SiC and TiC have self-sputtering coefficients which may exceed unity. Graphite exhibits high chemical sputtering rates, and BeO (along with other refractory compounds like SiC) is predicted to have its thermal conductivity reduced substantially by neutron radiation. The major concern with beryllium is the stability of the melt layer formed under disruptions. Several alloys including Cu, Zr, and V alloys, have been considered as heat sink materials. The reference heat sink material is a copper alloy.

(6) Erosion by physical sputtering is predicted to be mitigated by re-deposition of sputtered particles. Experimental data are, however, required on the rates of erosion and re-deposition.

(7) The basic design configuration of the limiter and divertor collector plate consists of a water-cooled heat sink composed of a high-thermal-conductivity structural material to which a surface material directly exposed to the plasma is attached. Such a duplex structure is required because, in almost all cases, materials that meet the sputtering requirements do not have the mechanical properties required for structural support. The preferred attachment concept is a high-strength, high-thermal-conductance bond.

(8) The detailed design of the impurity control components depends on the plasma edge conditions. There are different design solutions corresponding to the three edge temperature regimes considered. Each temperature regime is characterized by the pre-sheath plasma temperature, T_s, at the front surface of the limiter or divertor plate. At low T_s, where self-sputtering is no concern, medium- and high-Z materials can be exposed directly to the plasma. In general, the most desirable engineering designs are associated with this low-temperature regime. At medium T_s, a low-Z material, such as beryllium or graphite, must be used as the plasma-side material, and a high-thermal-conductivity structural material, such as a Cu alloy, must be used as the heat sink material. At the limiter leading edge, where particle energies

are $\lesssim 700$ eV, a high-Z material, like tungsten, can be considered as a plasma-side material for reducing sputtering erosion. At high edge temperatures, the limiter or divertor designs are similar to the medium-temperature designs, except that a low-Z material must be used at the limiter leading edges because of concern for high self-sputtering at the higher particle energies.

(9) The leading edge of the limiter presents key problems that require special design solutions. The cylindrical geometry of the leading edge generally results in more severe temperature and stress distributions than the rest of the limiter. Therefore, the heat flux to the leading edge should be kept lower than the heat flux to the top surface. For low-Z materials, the sputtering loss rate is much greater at the leading edge than at the front surface of the limiter.

(10) Stress and fatigue analyses indicate that the maximum allowable thickness of the plasma-side material is sensitive to the constraint imposed by the material on the heat sink. The stresses can be alleviated by reducing the width of the plasma-side tiles. Initial analysis of a structure with a high-strength bond indicates that a tile width of 2 cm is required to reduce the thermal fatigue stress range to an acceptable level. Additional theoretical and experimental work is required to determine the most appropriate way of controlling stresses in duplex structures.

(11) The lifetime of high-heat-flux components depends on the maximum allowable thickness for the plasma-side material and the material loss rate due to physical sputtering and disruption vaporization and melting. The predicted lifetimes vary with the plasma edge conditions and the selected plasma-side material. In the case of low edge temperature, the estimated lifetime for W-coated component is the lifetime of the reactor because of negligible material loss. In the case of medium and high edge temperatures, the predicted lifetime of Be-coated components is about two years at 50% reactor availability and at the reference disruption conditions. The lifetime can be quite sensitive to the assumed disruption conditions. Because of the uncertainties in the frequency, decay time constants, and energy deposition of disruptions, the predicted lifetime for plasma-side materials can vary by a factor of five. In addition, it is not known at this time what fraction of a melt layer formed during a disruption is lost from the surface. Additional theoretical and experimental effort is needed.

(12) Erosion of the first wall by charge-exchange neutrals is a key problem. In the case of the divertor, the charge-exchange flux is approximately uniform on the first wall, except perhaps near the divertor throat. In the case of the limiter, the charge-exchange neutrals are localized in the vicinity of the limiter. The rate and consequences of the transfer of eroded materials from the first wall to the limiter or divertor plate (or vice versa) need assessment.

The final recommendation is that the poloidal divertor should be the reference impurity control option. The pumped limiter should be retained as a design option. R and D should be pursued for both options to resolve uncertainties. The mechanical configuration and maintenance should accommodate both options.

13. MAJOR UNCERTAINTIES AND FUTURE EFFORT

13.1. Major uncertainties

The major uncertainties for impurity control are in the areas of:

(1) Plasma edge scrape-off conditions
(2) Physical sputtering
(3) Erosion/re-deposition
(4) Disruptions
(5) Irradiation effects
(6) Fatigue/crack propagation
(7) Tile/heat sink interface

Knowledge of the plasma scrape-off conditions is vital to the design of the impurity control system. The important parameters are the plasma edge temperature, particle density, and the e-folding distances for energy, power, and particle density. The design analyses have shown that a system can be designed for a particular set of edge conditions, but that the same system may be unacceptable for another set of conditions. In particular, high-Z materials appear to be the best choice as plasma-side materials for edge temperatures below 50 eV. They are, however, unacceptable at higher edge temperatures because of excessive self-sputtering. At present, it is believed that the most likely edge temperature operating range is $100\ \text{eV} \lesssim T_e \lesssim 400\ \text{eV}$, but there are considerable uncertainties in the expected conditions. Only low-Z materials are acceptable for the plasma-side tiles at edge temperatures above 50 eV.

The lifetimes of impurity control components are sensitive to the values for the physical sputtering coefficients of plasma-side materials. The areas of greatest uncertainties are the sputtering coefficients due to tritium ions, self-sputtering yields, particularly the energy at which self-sputtering exceeds unity for medium- and high-Z materials, sputtering yields for multicomponent materials such as SiC, and the sputtering coefficients for highly irregular and re-deposited surfaces. No laboratory data exist for tritium sputtering, and the predicted sputtering coefficients are expected to be accurate to only within a factor of two. The evaluation of self-sputtering coefficients is important to the determination of the permissible edge temperature ranges for medium- and high-Z materials. Finally, the actual plasma-side surfaces are either expected to be irregular or to have a modified

microstructure due to re-deposition and disruptions, and the different structures could result in different sputtering rates.

The lifetimes are also very dependent on high re-deposition rates for sputtered particles. Such high re-deposition rates have been predicted by computer models, but there are no data to confirm these calculations. The relative error in the lifetime estimates can be several times larger than the relative error in predictions of erosion and re-deposition rates. Substantial improvement in modelling of erosion/re-deposition is required and improvement in the data base for such calculations is necessary. Direct measurements of the erosion and re-deposition rates in a tokamak device are needed.

Disruptions could have a strong influence on the operation of impurity control and first-wall system because of potentially large vaporization and melt layer losses. The degree of material loss depends on frequency, energy density, and duration of the disruptions. In addition, the melt layer losses will depend on the accompanying magnetic and mechanical forces during the disruptions. All these quantities are uncertain at this time.

The bulk mechanical property data base for both plasma-side and heat sink materials is small, and therefore the response of these materials to the heat and irradiation conditions in INTOR cannot be predicted with certainty. Also, the duplex structure required for impurity control components introduces the need for an interface bond whose properties have yet to be determined. The properties of greatest concern are the fatigue/crack propagation properties and the effects of irradiation on swelling and embrittlement of the materials.

To this point, little attention has been devoted to the areas near the limiter that are subjected to a high charge-exchange neutral flux. Depending on the scrape-off conditions, these regions could experience high erosion rates and, therefore, limited lifetimes.

13.2. Future effort

The future effort should be aimed at obtaining sufficient understanding in the areas described in the previous section in order to successfully design and build an impurity control and first-wall system. The required effort can be divided into research and development (R and D) programmes and design/critical issue studies. The R and D programmes will be described in detail in Chapter XV and will only be summarized here. The R and D programmes consist of programmes aiming at a study of plasma-surface interactions and programmes intended for studying the engineering development, bulk properties, and long-term response of duplex structures. The plasma-surface programmes are in the areas of erosion/re-deposition, response of materials to plasma disruptions, and self-sputtering yields. The first two programmes incorporate both tokamak experiments and laboratory simulation experiments, whereas the last programme includes laboratory

experiments only. The materials development programmes consist of fabrication development, property evaluation of the interface bond, and bulk property evaluation of both plasma-side and heat sink materials. A programme to test the thermomechanical response of prototypical impurity control components is also proposed. Finally, development of in-situ techniques for re-coating eroded components is needed to find ways of extending their in-reactor lifetimes.

The design/critical issues studies can also be divided into the areas of plasma-surface interactions and engineering development of duplex structures. Additional effort is needed to upgrade the sputtering/re-deposition models to include time evolution of the surface geometry and to parametrically examine those areas where there are uncertainties in the data. The disruption studies require further effort to examine the interactions of vaporized particles with the disrupted plasma and to study the stability and kinetics of the melt layer. Furthermore, additional work is needed in determining the magnetic currents and forces that are produced during disruptions. Engineering development should focus on the effect of component geometry on the stresses within the structure and the influence of irradiation on the component lifetimes. The time evolution of properties and surface erosion should also be included in the evaluation of lifetimes. 2-D and 3-D finite-element computer studies will be useful in uncovering and resolving a number of key problems.

The area of impurity control must receive greater attention than in the past. Extensive effort is required in the areas of both physics and engineering, and innovative ideas should be encouraged.

REFERENCES TO CHAPTER VII

[1] European Community Contributions to the INTOR Phase-Two-A Workshop, Rep. Commission of the European Communities, Brussels (1982).

[2] Japan Contribution to the INTOR Phase-Two-A Workshop, Rep. Japan Atomic Energy Research Institute, Tokai-mura (1982).

[3] USSR Contribution to the INTOR Phase-Two-A Workshop, Rep. Kurchatov Institute, Moscow (1982).

[4] USA Contribution to the INTO Phase-Two-A Workshop, Rep. FED-INTOR/82-1, Georgia Institute of Technology, Atlanta (1982).

[5] INTOR GROUP, International Tokamak Reactor: Phase One (Rep. Int. Tokamak Reactor Workshop, 1980–81) International Atomic Energy Agency, Vienna (1982); see also Summary in Nucl. Fusion 22 (1982) 135.

[6] ROTH, J., BOHDANSKY, J., OTTENBERGER, W., Max-Planck-Institut für Plasmaphysik, Rep. IPP 9/26, Garching (May, 1979).

[7] ANDERSON, H.H., BAY, H.L., in Sputtering by Particle Bombardment (BEHRISCH, R., Ed.) Springer-Verlag (1981); J. Nucl. Mater. 93&94 (1980) 625.

[8] BOHDANSKY, J., J. Nucl. Mater. 93&94 (1980) 44.

[9] SMITH, D., BROOKS, J.N., POST, D.E., HEIFETZ, D., DSPUT: A Physical Sputtering Code for Fusion Applications, Argonne National Laboratory, ANL/FPP/TM-157 (1982); also Proc. 9th Symp. on Fusion Technology, IEEE Pub. No. 81CH195-2 NPS, (1981) 719.

[10] ROTH, J., BOHDANSKY, J., WILSON, K.L., Chemical Erosion of Carbon Due to Bombardment with Energetic Hydrogen Ions up to 1600°C (Proc. 5th Int. Conf. Plasma-Surface Interactions, May 1982, Gatlinburg).

[11] VIRGILIEV, Yu.S., et al., Preprint IAE-3248/8, Moscow (1980).

[12] MULLENDORE, A.W., WHITLEY, J.B., MATTOS, D.M., J. Nucl. Mater. 93&94 (1980) 486.

[13] SONE, K., et al., Surface Materials Consideration for Fusion Reactors, Japan Atomic Energy Research Institute, Rep. JAERI-M 82-156 (1982).

[14] CUPP, C.R., J. Nucl. Mater. 6 (1962).

[15] BROOKS, J.N., Erosion and Redeposition Analysis for Limiter and Divertor Impurity Control System, J. Nucl. Mater. (to be published).

[16] ZAVGORODII, A.Ya., et al., Kinetics of gas swelling in irradiated beryllium, Solid State Radiation Physics and Reactor Materials Research – USSR, DEPARTMENT OF COMMERCE, JPRS 53800 (1971) 268.

[17] MATTHEWS, R.B., J. Nucl. Mater. 51 (1974) 203.

[18] MATOLICH, J., et al., Swelling in Neutron-Irradiated Tungsten and Tungsten-25-Per cent Rhenium, Scr. Metall. 8 (1974) 837.

[19] WIFFEN, F.W., The Microstructure and Swelling of Neutron Irradiated Tantalum, J. Nucl. Mater. 67 (1977) 119.

[20] WILKES, R.S., Neutron-Induced Damage in BeO, Al203 and MgO – A Review, J. Nucl. Mater. 26 (1968) 137.